

Elemental dynamics and interactions in a carbonate-buffered, sulfatic and ferruginous lake

Daniel A Petrash¹, Christophe Thomazo², Astolfo Valero³, James J Valdes³, Karelys Umbría-Salinas³, Travis Meador⁴, Vladislav Chrastný⁵, and Kurt Konhauser⁶

¹Czech Geological Survey

²Université de Bourgogne

³Biology Centre of the Czech Academy of Sciences

⁴Biology Centre of the Czech Academy of Sciences, Institute of Soil Biology

⁵Czech University of Life Sciences

⁶University of Alberta

December 27, 2023

Abstract

Lake Medard is a recently established post-mining lake in the northwest of Czech Republic that displays significant concentrations of dissolved sulfate (dSO₄²⁻) and ferrous iron (Fe²⁺) in its density and redox stratified bottom water column. Siderite-buffered anoxic sediments, also rich in iron(III)-oxyhydroxides, underlie that water column characterized by limited labile organic substrates. This composition sustain a transitional redox state between nitrogenous/ferruginous and euxinic conditions. Our study focuses on the Lake Medard bottom water column elemental concentration profiles, sulfate-sulfur and -oxygen isotope compositions, bioactive ion concentrations, and planktonic microbiome data, combined with mineralogical and isotopic analyses of the upper anoxic sediments. This integrative approach reveals that the internal biogeochemical iron cycling is interlinked with that of nitrogen, sulfur and other redox sensitive metals. Minor seasonal oscillations in the monimolimnion redox potential impact mineral dissolution/(re)precipitation reactions, causing shifts in metal partitioning within anoxic sediments. Carbonate-buffered reactions appear to respond to a subsurface CO₂ flux thereby influencing monimolimnial alkalinity and dissolved inorganic carbon concentrations. These hydrochemical modifications shift the sedimentary redox signals, occasionally favoring carbonate over oxyhydroxide metal-binding processes. Our findings address the fate of newly formed sedimentary oxyhydroxides in a transitional redox-stratified water column featuring ferruginous conditions without quantitative sulfate depletion to provide insights on interlinked biogeochemical processes within a concise framework

Hosted file

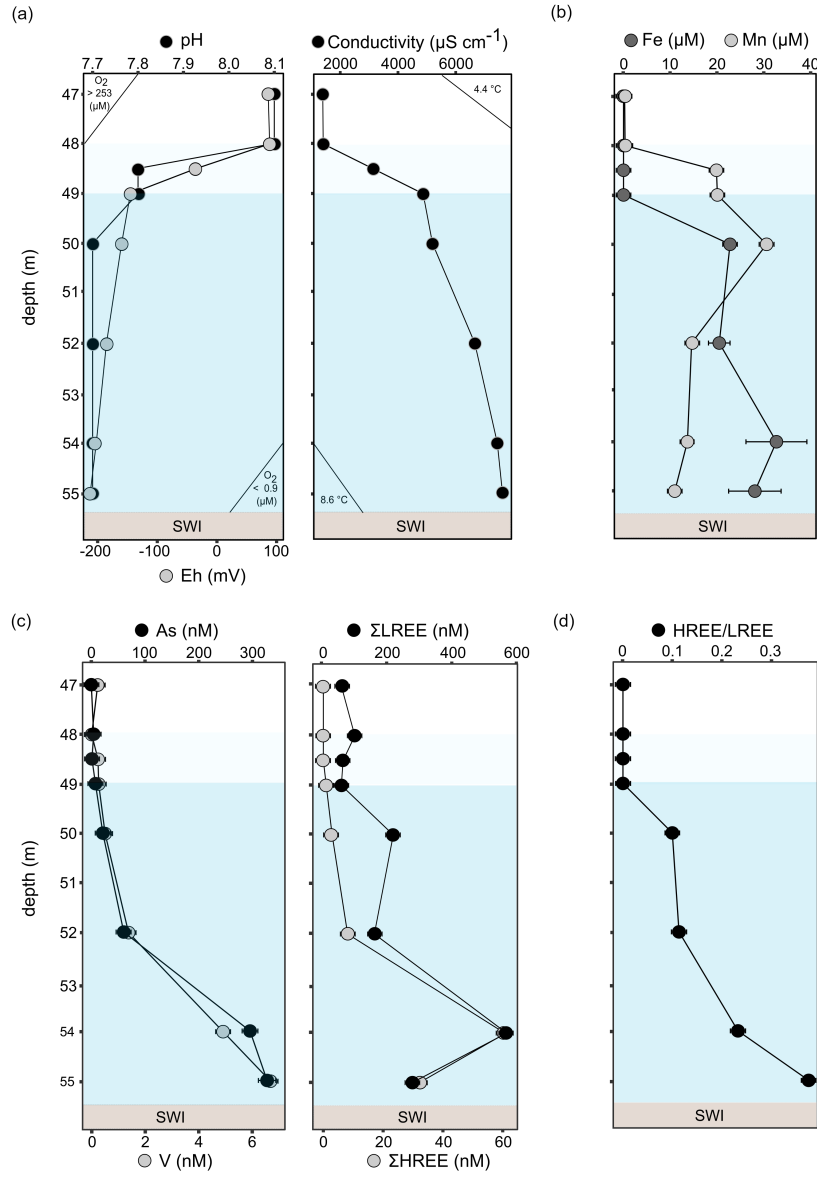
981940_0_art_file_11678606_s54d48.docx available at <https://authorea.com/users/708836/articles/693181-elemental-dynamics-and-interactions-in-a-carbonate-buffered-sulfatic-and-ferruginous-lake>

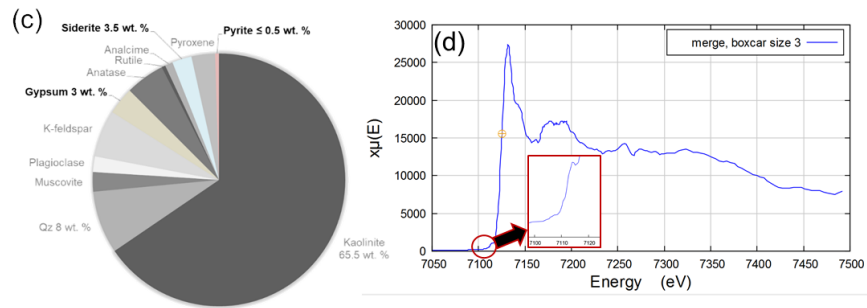
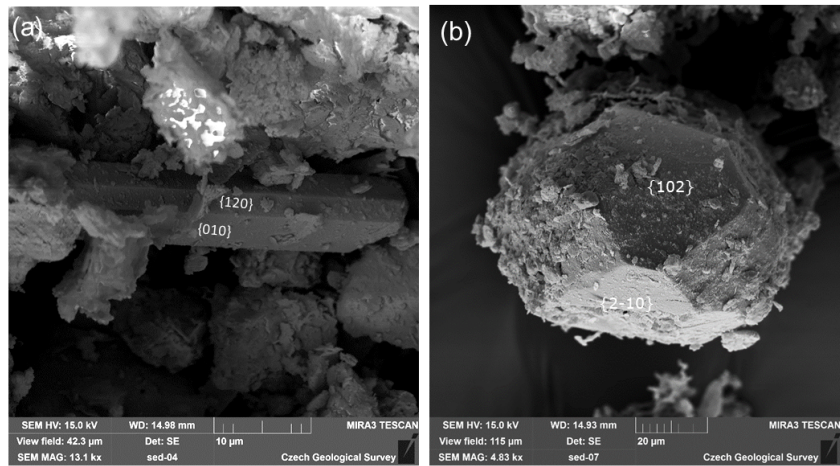
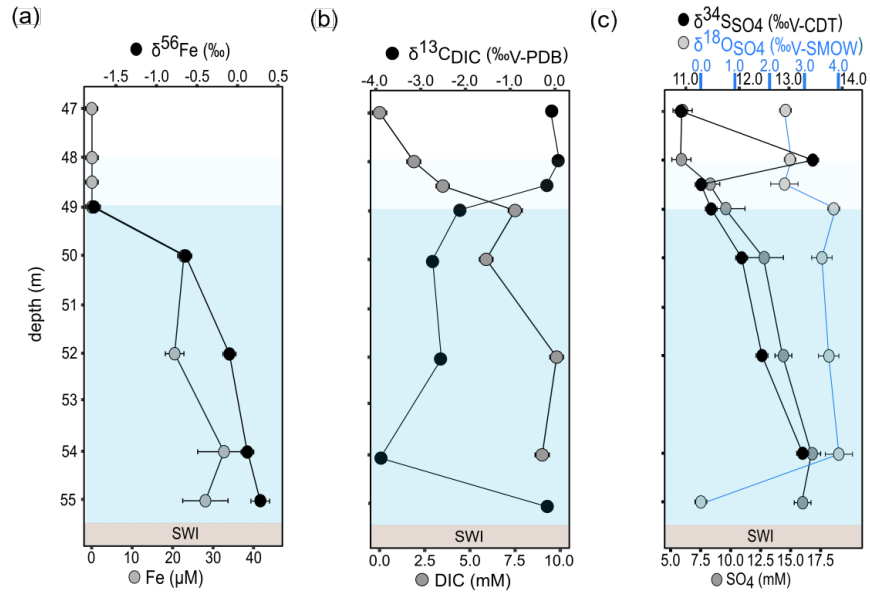
Hosted file

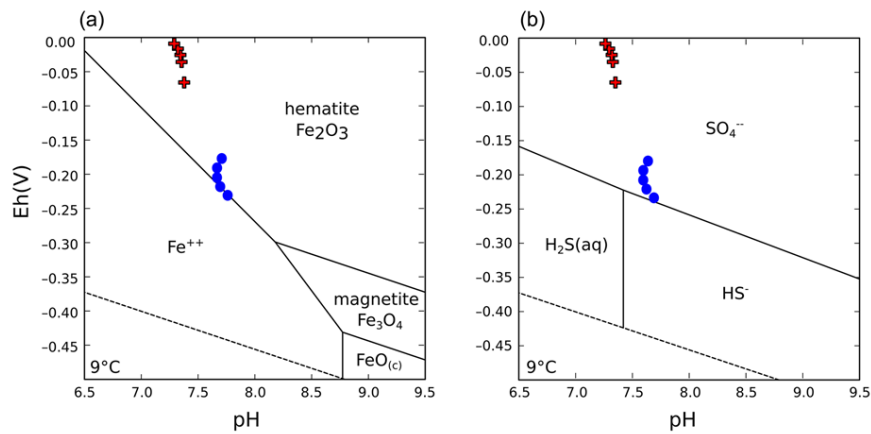
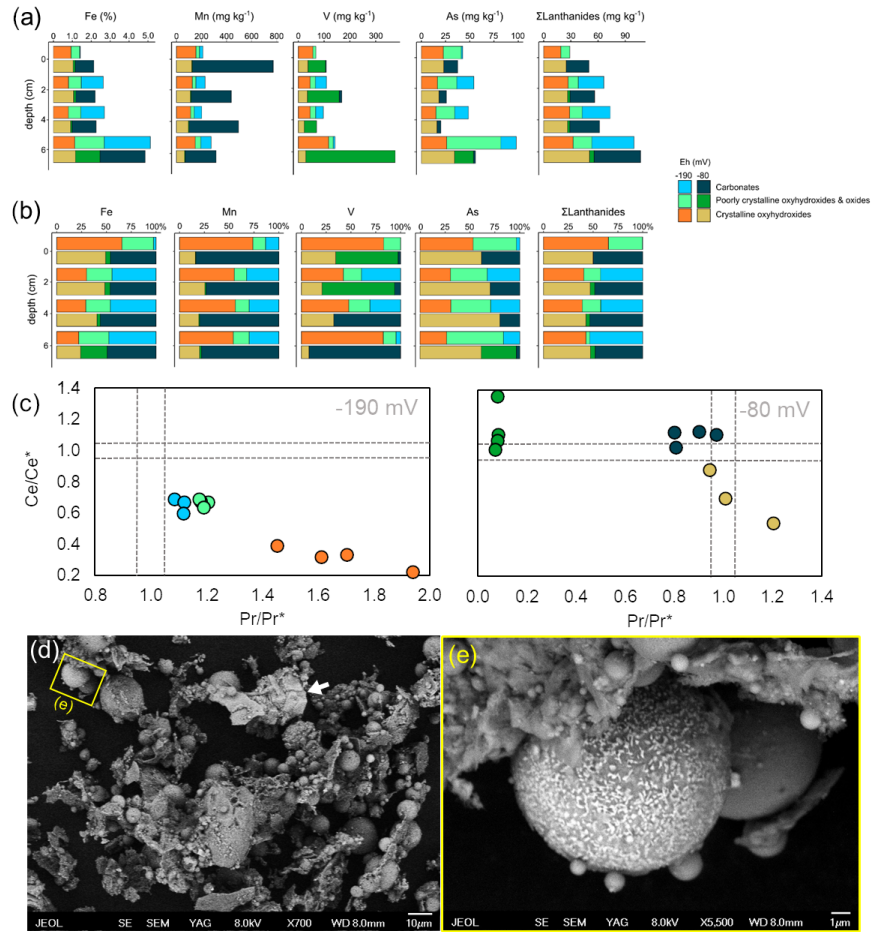
981940_0_supp_11678605_s5pd6j.docx available at <https://authorea.com/users/708836/articles/693181-elemental-dynamics-and-interactions-in-a-carbonate-buffered-sulfatic-and-ferruginous-lake>

Hosted file

981940_0_table_11678733_s5r9s0.docx available at <https://authorea.com/users/708836/>







1
2
3
4
5
6
7
8
9
10
11
12
13
14
15
16
17
18
19

Elemental dynamics and interactions in a carbonate-buffered, sulfatic and ferruginous lake

D.A.Petrash^{1,2}, C. Thomazo^{3,4}, A. Valero^{2,5}, J.J. Valdés², K. Umbría-Salinas², T.B. Meador^{2,5}, V. Chrastný⁶, K.O. Konhauser⁷

¹ Czech Geological Survey, 152 00 Prague 5, Czech Republic.

² Biology Centre, Czech Academy of Sciences, 37005 České Budějovice, Czech Republic.

³ UMR CNRS 6282 Biogéosciences, University of Burgundy, Dijon, 21000, France .

⁴ Institut Universitaire de France, Paris, 75000, France.

⁵ University of South Bohemia, Faculty of Science, 370 05 České Budějovice, Czech Republic/

⁶ Czech University of Life Sciences Prague, Czech Republic.

⁷ University of Alberta, T6G 2E3 Edmonton AB, Canada.

Corresponding author: Daniel A. Petrash (daniel.petrash@geology.cz)

Key Points:

- Lake Medard study offers insight into iron, sulfur, nitrogen cycling in redox-stratified waters
- Seasonal redox shifts affect mineral reactions; carbonate reactions and CO₂ flux alter lake chemistry
- Research aids understanding of microbial-mineral interactions in early Earth's oceans

20 Abstract

21 Lake Medard is a recently established post-mining lake in the northwest of Czech Republic that
22 displays significant concentrations of dissolved sulfate (dSO_4^{2-}) and ferrous iron (Fe^{2+}) in its
23 density and redox stratified bottom water column. Siderite-buffered anoxic sediments, also rich
24 in iron(III)-oxyhydroxides, underlie that water column characterized by limited labile organic
25 substrates. This composition sustain a transitional redox state between nitrogenous/ferruginous
26 and euxinic conditions. Our study focuses on the Lake Medard bottom water column elemental
27 concentration profiles, sulfate-sulfur and -oxygen isotope compositions, bioactive ion
28 concentrations, and planktonic microbiome data, combined with mineralogical and isotopic
29 analyses of the upper anoxic sediments. This integrative approach reveals that the internal
30 biogeochemical iron cycling is interlinked with that of nitrogen, sulfur and other redox sensitive
31 metals. Minor seasonal oscillations in the monimolimnion redox potential impact mineral
32 dissolution/(re)precipitation reactions, causing shifts in metal partitioning within anoxic
33 sediments. Carbonate-buffered reactions appear to respond to a subsurface CO_2 flux thereby
34 influencing monimolimnial alkalinity and dissolved inorganic carbon concentrations. These
35 hydrochemical modifications shift the sedimentary redox signals, occasionally favoring
36 carbonate over oxyhydroxide metal-binding processes. Our findings address the fate of newly
37 formed sedimentary oxyhydroxides in a transitional redox-stratified water column featuring
38 ferruginous conditions without quantitative sulfate depletion to provide insights on interlinked
39 biogeochemical processes within a concise framework.

40 Plain Language Summary

41 A unique lake formed in an old lignite mining area in the Czech Republic stands out due to high
42 levels of sulfate and iron in its deepest waters. We examined this lake's deep water column and
43 its bottom sediments, analyzing inorganic chemicals, minerals, and microorganisms. Our
44 research reveals that the interlinked iron and sulfur cycling in the lake system are vigorous.
45 Slight environmental changes in the oraganic-substrate depleted bottom water column can
46 significantly impact how iron mineral reactions in the sediments proceed. This study offers
47 insights into similar processes in ancient Earth's oceans, enhancing our understanding of Earth's
48 coupled geological and biological histories.

49 1 Introduction

50 A profound understanding of microbe-mineral interactions impacting Precambrian
51 shallow marine facies is necessary for accurately reconstructing Earth's early ocean redox
52 structure and better comprehending the evolution of geosphere-biosphere interactions. Several
53 recent research efforts have focused on investigating the sulfur cycle under ferruginous
54 conditions without a quantitative dSO_4^{2-} depletion (e.g., Mills *et al.*, 2016; Scholz, 2018; van de
55 Velde *et al.*, 2021). However, the transient state enabling such cryptic sulfur cycling to develop
56 is uncommon among the few modern mesotrophic lakes featuring either ferruginous or sulfatic
57 water columns. The former are frequently used as 'analogues' for understanding redox
58 stratification in ancient oceans (Koeksoy *et al.*, 2016). Those studies extrapolate, via analogy or
59 actualism, chemical and isotopic observations on modern ferruginous lake systems to interpret
60 geochemical signals preserved in Precambrian open-marine facies (Swanner *et al.*, 2020). Yet,
61 diagenetic models relying on modern low-sulfate lacustrine analogs offer limited insights into
62 Precambrian coastal areas where episodic interactions between ferruginous and sulfate-rich

63 waters likely occurred due to increased oxidative weathering of terrestrial sulfides. This
64 phenomenon became notably pronounced proceeding the initiation of sulfur redox cycling,
65 especially in coastal marine settings where photosynthetic microbial mats generated micromolar
66 levels of O₂ (e.g., Fakhraee *et al.*, 2019; Dreher *et al.*, 2021; Bayon *et al.*, 2022).

67 Lake Medard (LM), a recently formed post-mining lake in NW Czech Republic, provides
68 a unique opportunity to examine biogeochemical mechanisms and microbe-mineral interactions
69 in a nitrogenous, ferruginous, and sulfatic bottom water column overlying anoxic ferruginous
70 sediments. The latter contain ferric particles exported from the redoxcline as well Early Miocene
71 siderite redeposited in the lakebed that buffers the water column, maintaining an alkaline to
72 circumneutral pH. Sulfate, on the other hand, is delivered by groundwater recharge (Petraš *et*
73 *al.*, 2022). Here we relate spectroscopic concentration data of the chemically stratified bottom
74 waters of LM with analyses of the upper anoxic sediments. The solid phases in the sediments
75 were characterized using X-ray diffraction (XRD), Fe_{K1} absorption, and elemental
76 determinations conducted after a mineral-calibrated sequential extraction scheme targeting
77 reactive iron-bearing minerals (Poulton & Canfield, 2005; Claff *et al.*, 2010; Umbría-Salinas *et*
78 *al.*, 2021). These data were integrated with information on dissolved ions and volatile fatty acid
79 concentrations, $\delta^{34}\text{S}$ and $\delta^{18}\text{O}$ isotope ratio of dSO₄²⁻, $\delta^{56}\text{Fe}$ values of dissolved (residual) iron
80 (Fe²⁺), $\delta^{13}\text{C}$ and concentration determinations of dissolved inorganic carbon. Additionally, the
81 composition of the planktonic prokaryote community structure, based on amplicon sequence
82 analyses, was considered, along with $\delta^{34}\text{S}$ and $\delta^{18}\text{O}$ isotope ratios of authigenic gypsum and
83 pyrite, the $\delta^{13}\text{C}$ of carbonates present in the claystone-dominated overburden of the former mine
84 pit, and the $\delta^{18}\text{O}$ isotope ratios of the bottom lake waters.

85 This research sheds light on cryptic interlinked elemental cycles relevant to ancient
86 sedimentary systems and elucidates early diagenetic processes in LM sediments currently
87 undergoing alteration beneath a stratified ferruginous and sulfatic water column. We identify
88 complex (bio)hydrogeochemical patterns and trace element cycling that transcends regional
89 importance by shedding light on microbial-mineral interactions pertinent to the evolution of early
90 Earth's oceans. This contribution enriches a broader scientific understanding of biogeochemical
91 cycles, offering an actual perspective on Earth's geosphere and biosphere interplay throughout
92 history

93 **2 Materials and Methods**

94 *2.1 Water Sampling and analyses*

95 Samples were collected from the stratified LM bottom water column using a Ruttner
96 sampler at water depths ranging from 47 to 55 m below the surface. Prior to sampling,
97 physicochemical parameters of the water column were measured with a YSI 6600 V2-2 water
98 quality sonde (Xylem Analytics). Based on the probe information, the water column sampling
99 resolution was between 1 and 2 m. This design aimed to achieve a high-resolution understanding
100 of physicochemical properties near the redoxcline at the time of sampling (Fig. 1), approximately
101 48 ± 1 m, where the redox potential rate of change was higher with respect to depth. The water
102 sample aliquots underwent chromatography, optical and mass spectrometry, sequencing,
103 microscopy, and genomic analyses. Refer to Supporting Information for analytical details.

104 2.2 Sediment analyses

105 Replicate sediment cores, collected using an in-house made gravity corer, were analyzed
106 for mineralogy in the upper anoxic sediment column down to 8 cm below the SWI. The cores
107 were subsampled at a 2 cm-resolution in a custom-made glovebox under N-atmosphere,
108 immediately frozen using liquid N₂, and then freeze-dried before sample storage at -18 °C.

109 XRD qualitatively assessed sediment mineralogy, while a sequential extraction scheme
110 characterized the partitioning of Fe and Mn, the lanthanide series, and some redox sensitive
111 traces (V, As) into four operationally defined reactive solid phases: (i) Fe carbonates, (ii) easily
112 reducible poorly crystalline Fe(III) oxyhydroxides and manganese(IV) oxides, and (iii) reducible
113 crystalline Fe(III,II) oxyhydroxides (Poulton and Canfield 2005; Claff et al. 2010).

114 X-ray absorption slightly above the K₁-edge of Fe (7112.1 eV) evaluated the dominant
115 oxidation states of elements in the upper sediment minerals. The samples were stored in an
116 anoxic atmosphere of ≤5 parts per million (ppm) O₂ using a palladium catalyst and H₂ gas mix of
117 5% (Coy Labs) before analyses at a synchrotron hard X-ray beamline (MicroXAS beamline,
118 SLS-PSI).

119 Textural analyses of sediments were conducted using Field Emission Scanning Electron
120 Microscopy with Energy Dispersive X-Ray Spectroscopy. Additionally, total organic carbon
121 (TOC) contents were determined, and stable isotope analyses were conducted for δ³⁴S and δ¹⁸O
122 of gypsum, δ¹³C of siderite, and δ³⁴S_{CRS}. For comparison, the δ¹³C of siderite, and δ³⁴S of pyrite
123 present as authigenic phases in the Early Miocene terrigenous were considered. This comparative
124 approach allows determining the stability of isotopic signals upon diagenesis after re-deposition
125 in the modern lake. Refer to Supporting Information for details on sediment preparation,
126 analyses and instrumentation.

127 3 Study site

128 Located in the Sokolov mining district, roughly 19 km west-southwest of Karlovy Vary,
129 Czech Republic, the post-mining LM emerged through reclamation of the decommissioned
130 Medard-Libík open-cast lignite mine. Originally formed by infilled water diverted from the
131 nearby Eger (Ohře) river, LM now spans approximately 4.9 km² in areal extent, with maximum
132 depths between 48 and 60 meters below the surface at its west and central depocenters,
133 respectively. During the mid-2000s closure and abandonment of the LM mine pit, Fe and sulfate,
134 derived from sedimentary pyrite oxidation, leached into shallow and pit lakes as groundwater
135 filled the topographic post-mining depression (E. Murad et al., 2005; Enver Murad et al., 2003).
136 The hydrochemistry of the resulting shallow pit lakes was further influenced by runoff carrying
137 particles and solutes from weathered Early Miocene tuffaceous and carbonate-rich claystone at
138 the mine overburden. This lithology represents deposition that occurred in an Early Miocene rift
139 lake (Rojík, 2004). Authigenic minerals that accumulated in the shallow pit lakes preceding the
140 present-day, deeper post-reclamation lake included two-line ferrihydrite, schwertmannite,
141 goethite and jarosite; with detrital minerals such as kaolinite and mica also being present (Murad
142 & Rojík, 2003, 2005). The post-reclamation LM is characterized by density, temperature and
143 distinct redox stratification in its bottom water column (Fig 1a). The hydrochemistry of LM is
144 influenced by groundwater-rock interactions, aeolian deposition, and contemporary mineral

145 transformations of mine spoils and weathered, Early Miocene terrigenous redeposited in the
146 lakebed (Petrash et al., 2022).

147 **4 Results and Discussion**

148 4.1 Dissolved water column species, elemental cycling and upper anoxic sediment reactivity

149 4.1.1 Water column stratification features minor redox shifts affecting elemental cycling

150 LM exhibits a stratified water column (Fig. 1a) with a mixolimnion extending from the
151 lake surface to moveable depths approximating 44 to 48 meters. Below the mixolimnion is the
152 distinct hypolimnion transitional zone characterized by gradients in conductivity, salinity,
153 dissolved oxygen (O₂), pH, and temperature (Supporting Information, Table S1). An anoxic
154 monimolimnion lies toward the lakebed (Fig. 1a). This stratified layer is predominantly found in
155 the deepest central and western parts of the lake. In the eastern part, influxes of hypoxic, sulfate-
156 rich groundwater substantially modify the water column's redox structure; possibly resulting
157 from the seasonally absence of the anoxic zone, and with the redoxcline establishing in the
158 sediment below the SWI (Petrash et al., 2022). This intricate redox structure of the newly formed
159 water body was evident in the early water filling stages (Vrzal et al., 2011).

160 The bottom waters of LM are ferruginous and manganous, with comparable
161 concentrations of dissolved Fe(II) and Mn(II) around 30 μM (Fig. 1b, Table 1) — as determined
162 at the central sampling location (Supporting Information, Fig. S1). In the western depocenter,
163 these metal concentrations may exceed 100 μM (Petrash et al., 2018). Variability in transition
164 metals and sulfate concentrations in LM's bottom water column is attributed to fluid rock
165 interactions with weathered bedrock and/or a differential response to local hydrology, which
166 leads to laterally variable diffuse groundwater recharge from precipitation (Petrash et al., 2022).
167 The Miocene bedrock is argillaceous and contains pyritic coal seams. The embedded lignite
168 exhibits concentrations of lanthanides and arsenic (As) higher than the global average (Bouška et
169 al., 1999).

170 The solubility of metals governs variations in bottom water column conductivity, and
171 are impacted by redox potential fluctuations (Fig. 1a). As sedimentary Fe(III) and manganese
172 (Mn(IV,III) oxyhydroxides of redox-reactive phases with a high affinity for these metals undergo
173 reductive dissolution, dissolved lanthanides are mobilized from sediments. In consequence,
174 concentrations of these and other redox-sensitive element, such as vanadium, (V), increase
175 diffusively in the water column (Fig. 1c). Figure 1c-d further illustrates the impact of particulate
176 Fe and Mn reactivity on the availability of diffused, bottom water rare earth elements (REE).
177 Mobilization of light REE (LREE) occurs through reductive dissolution. Then upward diffusion
178 across the monimolimnion results in re-complexion of diffused LREE with partially stabilized
179 (i.e., selectively reduced) colloidal Fe(III)-bearing particles exported from the redoxcline, while
180 their heavy counterparts remain in solution. As the diffusive front, relatively enriched in heavy
181 REE (HREE), reaches the dysoxic zone in the hypolimnion, HREE become fully complexed by
182 metastable, poorly crystalline, and highly reactive Fe(III) precipitates. Consequently, their
183 dissolved concentrations rapidly decrease at the redoxcline (Fig 1d). Furthermore, proteins with
184 lanthanophilic properties secreted by homologous microorganisms identified in the microbiome

185 of LM, such as methylotrophic bacteria, may also play a role (Valdes et al., 2024) thereby
 186 warranting further scrutiny regarding relevance and extent.

187 *4.1.2 The carbonate budget*

188 LM's bottom water column exhibits a pH gradient ranging from alkaline to circumneutral
 189 (8.2 to 7.4 units), decreasing with increasing depth (Fig. 1a). Simultaneously, dissolved inorganic
 190 carbon (DIC) concentrations substantially increase from 1.9 to 9.8 mM (Fig. 2b, Table 1).
 191 Alongside this alkalinity increase, DIC's $\delta^{13}\text{C}$ values decrease, suggesting the influence the
 192 lakebed's ^{13}C -depleted hydrochemical input on the monimolimnial carbon reservoir (Fig. 2b).
 193 The dissolution of redeposited Miocene Fe-dolomite and siderite in the modern lakebed can
 194 buffer sediment pH while providing substantial carbonate alkalinity to the bottom density
 195 stratified waters. On the one hand, dolomite, once abundant in the Miocene "detrital" sediment
 196 source to LM, is now < 0.5 wt. % (i.e., the detection limit of semi-quantitative XRD). On the
 197 other hand, less soluble siderite accounts for about 4 wt. % of the total mineralogy.

198 The bulk $\delta^{13}\text{C}$ values of LM's anoxic sediments are $+6.4 \pm 0.3$ ‰ ($N = 6$), primarily from
 199 siderite. This contrasts with Miocene carbonate-bearing claystone in the former mine
 200 overburden, where siderite has $\delta^{13}\text{C}$ values in the range $+8.49$ to $+10.64$ ‰ ($N=6$). In contrast,
 201 Miocene dolomite has a broader range of $\delta^{13}\text{C}$ values between $+1.41$ and $+7.48$ ‰ ($N=9$).
 202 Therefore, the LM's siderite is depleted in ^{13}C by 2 to 4 ‰ compared to the mean $\delta^{13}\text{C}$ values of
 203 Miocene siderite. Given the observed $\delta^{13}\text{C}$ offset of $+9.1$ ‰ to $+10.9$ ‰ regarding the
 204 monimolimnial DIC (Fig. 2b), a small proportion of siderite likely forms on the lakebed,
 205 influencing the bulk sediment $\delta^{13}\text{C}$ signature towards less positive values. However, the bulk of
 206 this carbonate phase is thought to be redeposited and sourced from Miocene strata as determined
 207 by using a simple mass balance approach (see below).

208 To explain the relatively ^{13}C depleted DIC, a source other than dissolution of detrital
 209 carbonates must be considered. The DIC in LM bottom waters might be influenced by an active
 210 regional influx of geogenic CO_2 with a modal signature $\delta^{13}\text{C}$ value between -1.8 and -4.0 ‰
 211 (Geissler, 2005; Weinlich et al., 1999). This geogenic CO_2 flux, migrating through the Eger rift
 212 fault systems, has regionally permeated the upper crust and its volcano-sedimentary cover since,
 213 at least, the Early Miocene (Mach et al., 2017; Rapprich et al., 2023). Furthermore, a geogenic
 214 CO_2 flux can moderately decrease the pH (~ 0.4 units) of the water column (Fig. 1a.), consistent
 215 with the acidifying nature of dissolved CO_2 , forming carbonic acid in the lake water, which
 216 readily dissociates to release protons thereby lowering the pH while increasing alkalinity (Fig.
 217 2b).

218 Another potential source of ^{12}C in the monimolimnion is organotrophic respiration,
 219 which, depending on dominant metabolic pathways and the type of labile organic matter
 220 available, might lead to a moderate decrease in pH (Gallager et al., 2014; Soetaert et al., 2007,
 221 Middleburg, 2019). Sedimentary organic matter in LM exhibits a narrow $\delta^{13}\text{C}$ range of $-27.9 \pm$
 222 0.1 ‰ ($N = 6$). Using this value and the mean $\delta^{13}\text{C}$ values in carbonates from the anoxic sediment
 223 in a simple linear mixing model (Phillips and Gregg 2001) suggests that about 70 ± 5 % of the
 224 DIC originates from the dissolution of sedimentary carbonates. The rest is derived from other
 225 CO_2 sources, must more likely geogenically dominated given LM's current oligotrophic state. To
 226 discern the relative contributions of geogenic sources and organotrophic respiration, it is crucial

227 to quantify how much DIC can be produced by organotrophic respiration pathways operating
 228 within the lakebed and to analyze its stable carbon isotope signature. Efforts towards this end,
 229 akin to those detailed in Havas et al., 2023a,b, are currently in progress. Nonetheless, this aspect
 230 extends beyond the primary focus of this study and represents an avenue for future research that
 231 will build upon our current findings.

232 **4.2 Dissolved sulfate regeneration, consumption and/or solid phase incorporation**

233 Another distinctive feature within the redox and carbonate-buffered LM stratified waters
 234 are the relatively high sulfate concentrations, ranging from 5.2 to 17.5 mM, that exhibit a notable
 235 increase with depth. A slight decrease in dSO_4^{2-} levels (0.8 mM) approaching the SWI (Fig. 2c)
 236 suggests an ongoing sulfate reduction within the monimolimnial waters. Examining the $\delta^{34}\text{S}$
 237 values of dSO_4^{2-} concentrations, ranging from +10.9 to +13.4 ‰ (Fig. 2c), statistically
 238 significant positive correlation emerges with the $\delta^{34}\text{S}$ values of the residual sulfate (Pearson
 239 coefficient ≈ 0.970 , $p\text{-value} < 0.01$). This correlation suggests a direct linear relationship between
 240 these two parameters (Table 1). Such an apparent correlation implies differential microbial
 241 activity, sulfide reoxidation, and/or discrete sulfur sources with distinct isotopic compositions
 242 influence the variability of $\delta^{34}\text{S}$ and sulfate concentrations in the stratified LM's water column
 243 (Fig. 2c).

244 A covariation becomes apparent between $\delta^{56}\text{Fe}$, of residual Fe, and $\delta^{34}\text{S}$, of residual
 245 sulfate (cf. Fig. 2a and 2c). The dataset in Table 1 shows a robust correlation between Fe and
 246 sulfate concentrations (Pearson coefficient = 0.952, $p\text{-value} = 0.01$) mirroring similar statistical
 247 relationships between their isotopic compositions ($\delta^{56}\text{Fe}$ and $\delta^{34}\text{S}$, Pearson coefficient ≈ 0.947 , $p\text{-}$
 248 $p\text{-value} < 0.05$). These findings suggest a closely linked behaviour of dissolved Fe and sulfate in
 249 the LM water column. The observed covariation supports precipitation of monosulfide, some
 250 serving as precursors for dispersed microcrystalline pyrite (Fig. 3a). Archer & Vance (2006)
 251 observed a positive $\delta^{56}\text{Fe}\text{-}\delta^{34}\text{S}$ correlation in Late Archean sedimentary pyrite interpreted to
 252 reflect simultaneous dissimilatory Fe and sulfur reduction. We confirmed this correlation in our
 253 lake sediments and suggest it mirrors transient sulfatic and ferruginous conditions in the water
 254 column during iron snow deposition and alteration, indicating a dynamic interplay in early
 255 diagenesis of reactive Fe phases.

256 Accessory and minor amounts of pyrite and gypsum were also detected in the anoxic
 257 sediment (Fig. 3b). The isotopic $^{34/32}\text{S}$ composition of gypsum, referred to as $\delta^{34}\text{S}_{\text{Gy}}$, ranged from
 258 -13.9 to -9.6 ‰, which contrasts with the average $\delta^{34}\text{S}$ values of dSO_4^{2-} in LM bottom waters
 259 (approximately +12.8 ‰; Fig. 2c; Supporting Information, Fig. S2a). This discrepancy indicates
 260 that $\delta^{34}\text{S}_{\text{Gy}}$ recorded a significant fractionation process and that gypsum is not in a redeposited
 261 phase as siderite. The apparent fractionation recorded by gypsum, however, will only operate if
 262 the mineral is the direct product of the SO_4^{2-} anions in the LM water column reacting with Ca^{2+}
 263 released from the sediments, i.e., from carbonate mineral dissolution. Alternatively, the mineral
 264 is not directly precipitated from dSO_4^{2-} in the LM water column, where it remains unsaturated
 265 (Table 3), but rather forms from a SO_4^{2-} source that is rather restricted to the sediments.
 266 Noteworthy, is that the $\delta^{34}\text{S}_{\text{Gy}}$ values are relatively closer to those of sedimentary sulfides, (-35.1
 267 $< \delta^{34}\text{S}_{\text{CRS}} < -23.0$ ‰; Petrush et al., 2022), implying a common process during authigenesis.

268 At the SWI, the presence and isotopic signature of pyrite reveal an intricate
 269 (hydro)biogeochemical interplay. Pyrite exhibits an isotopic offset of ~38 ‰ (expressed as
 270 $^{34}\epsilon_{\text{CRS-SO}_4}$) relative to the mean $\delta^{34}\text{S}$ of dissolved SO_4 in the monimolimnion. This offset may
 271 indicate isotopic fractionation during incomplete microbial sulfate reduction within an open-
 272 system oxidative sulfur cycle (Johnston et al., 2014; Zerkle et al., 2016). Microbial sulfate
 273 reduction is limited in this context, as only dispersed amounts of pyrite form. The isotopically
 274 enriched Miocene pyrite, exhibiting $\delta^{34}\text{S}_{\text{CRS}}$ values of between +8 and +27‰ (median 16‰)
 275 (Supporting Information 2, Figure S2b), is unlikely a detrital source component for this pyrite,
 276 implying the presence of specialized SR bacterial populations capable to drive pyrite precipitation.
 277 Their activity, however, has minimal effect on the monimolimnion concentrations of dSO_4^{2-} or
 278 Fe^{2+} (Brüchert, 2004; Canfield, 2001). These bacteria could completely oxidize their preferred
 279 labile organic substrate and are thus limited by its scarcity—available in nM concentrations or
 280 below the quantifiable limit at the LM monimolimnion. These substrates are, in decreasing order
 281 of abundance, acetate, formate, pyruvate, and lactate (Petrasch et al., 2022).

282 The solid phase $\delta^{34}\text{S}$ values indicate that gypsum in the upper sediment may have
 283 incorporated sulfide-derived sulfate. This sulfate moiety in gypsum is ^{18}O -enriched by about 2.0
 284 ± 0.6 ‰, relative to the mean $\delta^{18}\text{O}_{\text{SO}_4}$ of the monimolimnion. This magnitude of enrichment
 285 aligns with $\Delta^{18}\text{O}_{\text{SO}_4\text{-H}_2\text{O}}$ values observed in anaerobically oxidized pyrite products (Balci et al.,
 286 2007). Since the $\delta^{18}\text{O}$ of the anoxic ambient water ranges between -6.1 and -6.7 ‰, with a mean
 287 of -6.5 ‰, then the magnitude of solid phase ^{18}O enrichment in gypsum falls within the expected
 288 range when sulfate is partially derived from sulfide oxidized by ferric iron (Böttcher et al., 2001,
 289 2005; Böttcher and Thamdrup, 2001), exemplified by the reaction:



291 Consistent with this interpretation, an oxygen isotope effect ($^{18}\epsilon_{\text{SO}_4\text{-amb. wat.}}$) of +9.3 to
 292 +10.7 ‰ can be calculated, supporting the notion that S^{-2} oxidation likely involves S-
 293 disproportionation (Brunner et al., 2005; Bottrell and Newton 2006). The sulfur and oxygen
 294 isotopes near SWI and below sulfate are decoupled, indicating a quantitative cycling within the
 295 sediments. Disproportionation involves partial S transition from its oxidized to its reduced state
 296 through an intermediate valence state that later disproportionate into sulfate and sulfide. The
 297 short-lived, intermediate products (e.g., thiosulfate) rapidly exchange oxygen atoms with water
 298 molecules in the anoxic porewater system, before returning to the oxidized dSO_4^{2-} porewater
 299 pool. This porewater sulfate reacts with Ca^{2+} solubilized during localized carbonate dissolution,
 300 resulting in the observed relative ^{34}S -depleted equant gypsum microcrystals (Fig. 3b). The rapid
 301 reaction of sulfide with FeOOH constantly exported from the redoxcline, thus prevents sulfide
 302 from substantially accumulating in the sediment, while low levels of dissolved sulfide are
 303 maintained in LM bottom waters, e.g., ≤ 0.3 μM (Petrasch et al., 2018, 2022).

304 **4.3 Metal partitioning in the lakebed**

305 Sediment composition and metal partitioning dynamics within the upper anoxic
 306 sediments were examined using a suite of X-ray analyses. XRD revealed a sedimentary matrix
 307 predominantly composed of kaolinite, mica, and quartz. Embedded within this clayey matrix are
 308 minor constituents such as rutile, analcime, siderite and gypsum. The latter minerals each
 309 constitute approximately 3-5 wt. %. Pyrite was also present in accessory amounts (≤ 1 wt. %)

310 (Fig. 3c). The mineralogy of the present-day LM closely resembles that observed in the Miocene
311 lacustrine facies in the overburden of the former mine (Murad & Rojik, 2003; Kribek et al.,
312 2017)

313 X-ray absorption near-edge structure (XANES) at the Fe_{K1} -edge indicated the presence of
314 FeOOH polymorphs, notably goethite (Fig. 3d). These polymorphs form organo-mineral
315 aggregates, as observed through scanning electron microscopy of the upper sediment strata (Fig.
316 4c). The distribution of FeOOH phases in the sediment pile suggests that reductive dissolution
317 diminishes the prevalence of amorphous and poorly crystalline Fe(III) oxide phases delivered
318 from the redoxcline via water column settling but favoring the accumulation of more crystalline
319 forms. Additionally, our $\delta^{56}\text{Fe}$ isotopic data (illustrated in Fig. 2a) strongly suggest that
320 metastable monosulfide precursors can precipitate near the SWI to later undergo limited
321 stabilization to disperse pyrite, which relative abundance is near the detection limit of the semi-
322 quantitative XRD technique (Fig. 3b-c). On this note, the sedimentary $\text{Fe}_{\text{py}}/\text{Fe}_{\text{HR}}$ indicator, as a
323 measure of the extent to which highly reactive iron (Fe_{HR}) is converted to pyrite (Raiswell *et al.*,
324 2018), was found to be ≤ 0.25 . Consistent with the anoxic (ferruginous) character of sediments at
325 the lake floor, the indicator of anoxicity ($\text{Fe}_{\text{HR}}/\text{Fe}_{\text{T}}$) is > 0.7 (Petrash *et al.*, 2022).

326 Results of aqueous-mineral equilibrium calculations, shown in Table 3, indicate the
327 potential for certain minerals to precipitate from the overlying water column. These calculations,
328 conducted using the geochemical modeling software PHREEQC, assess the saturation indices of
329 various minerals under two distinct aqueous redox potential regimes observed. In the
330 monimolimnion, peak Eh can oscillate between -210 mV and -80 mV, reflecting the dynamic
331 hydrological state of the stagnant lake is modulated by seasonal precipitation patterns and,
332 subsequently, groundwater recharge. The comparatively higher Eh value of -80 mV is transient,
333 manifesting only after seasonal rainfall events. Nonetheless, the less reductive monimolimnial
334 conditions are ephemeral, with the redox potential near the SWI reverting to a more consistent
335 *ca.* -210 mV due to the diminishing influence of groundwater recharge (Umbria-Salinas *et al.*,
336 2021).

337 Most elements are relatively enriched when normalized against standard geochemical
338 baselines (e.g., Wedepohl, 1995) or against concentrations measured in local sedimentary
339 sources to the modern lake system (Supporting Information, Fig. S3). The thermodynamically
340 stable phases (i.e., at chemical equilibrium) in LM's bottom water column (Fig. 4). To evaluate
341 the sedimentary response to the redox shifts detected within the monimolimnion, we
342 implemented a sequential extraction protocol targeting highly reactive Fe-bearing minerals. Our
343 mineral-specific concentration profiling focused on the partitioning of Mn, REE, V, and As (Fig
344 5-ab, Table 2).

345 The redox reactivity of Mn is notable, with its aqueous availability and complexation
346 dynamics altered by Eh transitions within the LM water column (Fig. 1b). In addition, Mn plays
347 a prominent role in the transfer of other trace metals, such as REE, from the water column to the
348 SWI and their subsequent uptake by authigenic phases subjected to burial (Tribouillard *et al.*,
349 2006). Our data suggest that Mn(IV,III) is readily reduced in the water column and subsequently
350 associates in its reduced state with reactive particulate phases (i.e., more stable Fe-
351 oxyhydroxides) that finally reach the lake floor. Under more reductive conditions, this
352 association is evidenced by preferential partitioning into the carbonate fraction, hinting at

353 decreased export of poorly crystalline, highly reactive phases and diminished complexation
354 capacity of the reducible oxide phases that can effectively exert some Mn(II)-binding. When the
355 redox potential gradient in the bottom water column is less marked, however, Mn(II)
356 complexation with carbonate is readily favoured (Fig. 5a-b, Table 2).

357 The sediment core profiles further reveal that under the two documented redox potentials, REE
358 exhibit sediment partitioning patterns that compare best with those of Mn. Analysis of positive
359 cerium anomalies points to enrichments of Ce(III) into carbonates under the less reductive
360 conditions (Fig. 5c). Concurrently, negative anomalies indicate solubilization of redox-sensitive
361 Ce(III) bound to easily reducible amorphous oxides, which can in turn be more profusely
362 exported from the redoxcline at times when the water column exhibited more marked Eh
363 gradients. This reflects on mobilization of redox sensitive elements such as cerium at the SWI
364 and below (Fig. 5c). The observed phase distribution patterns emphasize the relative stability of
365 authigenic and sedimentary carbonates for water column-induced changes in REE partitioning,
366 underscoring their importance in the geochemical framework of sedimentary redox-sensitive
367 interpretations (Umbría-Salinas et al., 2021).

368 In contrast to the other redox-sensitive proxies considered here, V and As exhibit
369 distinctive behaviors in response to the dynamic redox gradients of the water column. At the
370 highest Eh observed, V demonstrates a notable affinity for poorly crystalline oxyhydroxides, an
371 interaction that appears to be intensified at times when an increased proportion of reactive
372 oxyhydroxides, amenable to be partially stabilized in transit to the SWI (Posth *et al.*, 2014), can
373 be more profusely generated at the redoxcline. Evidenced by the depth profiles depicted in Fig.
374 5a-b, a lower water-column Eh gradient can favour binding of V to crystalline oxyhydroxides.
375 Enrichments of V in the upper sediment layers, associated with crystalline oxyhydroxide, are
376 likely due to changes in mobilization and particulate binding of the vanadate ion $\text{VO}_2(\text{OH})_2^{2-}$
377 under conditions of increased redox potential in the water column. Below a depth of 2 cm, V
378 increasingly associates with carbonates a times when redox potential is decreased (Table 2).

379 The pattern displayed by As displays contrasts with V, which potentially indicates a more
380 complex set of interactions within the sediment matrix. While As tends to associate with
381 carbonates during marked redox transitions at or near the SWI, (illustrated in Figure 5a-b), in the
382 upper sediment layers, at times when redox buffering by the water column increases, As shifts
383 towards preferential binding with Fe-oxyhydroxides. This behaviour suggests variable
384 interactions with the abundant crystalline Fe(III) phases in the deeper sediment layers, a probable
385 vestige of the geochemical milieu preceding the lake's formation or differential. The reactivity of
386 As in the upper sediment is due to currently unaccounted biogeochemical factors, such as
387 underestimated water column-based microbial As metabolisms (Saunders et al., 2019) or
388 oxidative process driven by electron transfer mechanism involving particle-cell interactions
389 (Valero, Jan & Petrash 2023). Notably, the lower strata of modern lake sediments, rich in jarosite
390 (Murad & Rojik, 2003), exhibited high affinity for As (Karimian et al., 2017). Over time,
391 however, jarosite altered, transitioning to goethite, which now dominates the lakebed
392 geochemical landscape (Figs. 3d and 5e).

393 **4.4 Elemental cycling and microbial community structure at LM**

394 The concentration profiles of dissolved metal at LM reveal a vigorous internal cycling in
395 the water column, impacting recently deposited, highly reactive sediments. This cycling
396 encompasses a sequence of mineralogical transformations influencing the fate of redox sensitive
397 metals and metalloids traversing the redox-stratified water column, alongside colloidal Fe and
398 Mn. Reactive aggregates on the sediment surface serve as a habitat for bacteria colonizing early
399 formed mineral clusters. As these aggregates descend across the stratified water column, the
400 activity of bacterial communities (e.g., Fe- and Mn-reducers and -oxidizers) colonizing the
401 surfaces induce the dissolution and re-precipitation/stabilization of amorphous phases into poorly
402 crystalline phases (Posth et al., 2014). This transformation may progress to partial stabilization
403 into metastable, more crystalline forms, such as lepidocrocite. This latter FeOOH polymorph is
404 found at the SWI, albeit less abundant than goethite (Fig. 3d).

405 During transit to the SWI, microbial-mineral aggregates interact with various compounds,
406 such as scarcely available organic substrates, humic substances, and planktonic prokaryotes.
407 Some of these prokaryotes may be capable of transferring electron to and from the conductive
408 Fe(II, III)-bearing particles (see Valero et al., 2024). Reflecting other systems in the past, LM
409 represents a dynamic ecosystem where microbial interactions in the water column play a central
410 role in the cycling not only of Fe, S and C but also other interlinked elements (Posth et al., 2014).

411 Genomic analyses (ENA accession: PRJEB47217) underscore the prevalence of δ - and β -
412 proteobacterial groups in the LM microbial community. In the upper hypolimnion, members of
413 the *Gallionellaceae* family are integral to an Fe-oxidizing-nitrate-reducing community inducing
414 metastable Fe(III) precipitation. These precipitates descend and partially dissolve in the
415 monimolimnion due to the activity of Fe reducers like *Geobacter* spp., releasing metals
416 complexed to the aggregates back in the solution. Despite sulfate reducers near the SWI,
417 microbial activity remains restrained owing to a general lack of labile organic substrates. This
418 significantly restricts sulfide production until relative formate enrichment, as demonstrated by
419 Valero et al. (2024), which stimulates their activity, results in precursory pyrite formation.
420 Recent experiments also show that in LM's anoxic waters, distinct Gallionellaceae may engage
421 in a extracellular electron transfer, impacting sulfur, Fe, and nitrogen cycling with the
422 involvement of other EET-capable microbes, for example *Desulfobulbaceae*. This interaction
423 appears crucial for stabilizing Fe(III) minerals and influencing As complexation (Valero et al.,
424 2023).

425 **5 Summary and Conclusions**

426 We utilized spectroscopic methods to analyze the gradients of dissolved C, N, S, Fe, and
427 Mn in the redox-stratified LM, revealing it features a unique intermediate state between
428 nitrogenous and euxinic conditions. This state results from active sulfur and iron co-recycling,
429 influenced by the reducible Fe and Mn proportions available at the from anoxic sediments.
430 Analyzing the interplay of microbial dynamics, mineral transformations, and redox-sensitive
431 geochemical cycles in the post-mining LM offers a novel perspective on the complex
432 interactions shaping the evolution of early biosphere-geosphere interactions. Through this
433 research, we present a comprehensive model bridging the gap between modern analogs and
434 ancient marine settings, emphasizing the dynamic nature of geochemical processes and their
435 enduring impact on Earth's history.

436 Outlined below are key observations and interpretations governing the geochemical and
437 geomicrobiological processes within the LM redox-stratified water column. Additionally, we
438 highlight their consequential impact on elemental cycling and mineral partitioning in the
439 stratified water column and its underlying anoxic sediments.

- 440 1. The density and salinity-stratified water column of LM exhibits redox gradients, particularly
441 across the anoxic monimolimnion. In the upper anoxic sediments, the redox-sensitive metals
442 content bound to minerals subjected to reductive dissolution substantially shift due to
443 mobilization from seasonal redox potential changes in the monimolimnion.
- 444 2. The ^{56}Fe proxy validates a water-column centered Fe cycling dynamics, corroborating
445 reductive dissolution and re-precipitation processes that affect metal solubility within the LM
446 bottom water column and the SWI. Sulfate reduction and potential monosulfide precipitation
447 occurs near the SWI. As supported by $\delta^{34}\text{S}$, $\delta^{18}\text{O}$ data, re-oxidization of most sulfide
448 potentially involves S disproportionation. These lakebed processes result in ^{34}S -depleted
449 gypsum compared to dSO_4^{2-} in the monimolimnion, yet it reflects the $\delta^{18}\text{O}$ signature of the
450 ambient anoxic water. This phenomenon points to a mixed source sulfate, although
451 dominated by sulfate sourced from the bedrock.
- 452 3. Redeposited Miocene carbonates, particularly siderite, buffer the LM bottom water pH, while
453 an active regional influx of geogenic DIC flux influences dissolved carbonate ion budgets
454 and carbonate co-precipitation potential at the lakebed. Spectrometry from XRD and XANES
455 reveal minor changes in redox potential of the bottom waters resulting in variations in the
456 production and export of newly formed amorphous and metastable oxyhydroxides at the
457 redoxcline to the sediments.
- 458 4. Dominance of proteobacterial groups and identified microbial communities highlight their
459 pivotal role in metal respiration, electron transfer mechanisms, and biogeochemical cycling
460 of Fe, S, and C among other interlinked elements. Distinct *Gallionellaceae* species, and
461 similar syntrophic microbes capable of engaging in EET from Fe(III)-phases, are potentially
462 integral in such interactions that lead to Fe(III) mineral stabilization within anoxic sediments
463 and mediating metal cycling within the redox stratified water column.
- 464 5. Reductive dissolution, re-complexation, and co-precipitation are primary processes
465 governing the solubility dynamics of metals, such as Fe, Mn, V, As, and REE, within the LM
466 water column and the underlying highly reactive, redox- (ferrous Fe) and carbonate-buffered
467 anoxic sediments. Incorporating observations on bottom water column redox fluctuations
468 provides a nuanced perspective on fluid-rock/mineral interactions and biogeochemical
469 cycling in stratified aquatic systems.
- 470 6. Redox fluctuations, particularly Fe speciation, significantly influence the behavior of reactive
471 solutes through Fe redox cycling that are intricately linked with the cycling of nitrogen,
472 sulfur, and other redox-sensitive metals. Minor seasonal changes in the bottom water column
473 redox potential can significantly impact interactions involving mineral dissolution and
474 (re)precipitation reactions, as well as the metabolic functioning of the lake. Furthermore,
475 subtle shifts in the redox state of the bottom water column can induce transients in metal
476 partitioning within anoxic sediments, influenced by carbonate-buffered reactions driven by

477 subsurface CO₂ flux, altering monimolimnial alkalinity and dissolved inorganic carbon
478 levels.

479 **Acknowledgments**

480 The authors have no conflict of interest to declare. Our sincere thanks go to Stefan Lalonde
481 (Université de Bretagne Occidentale) for conducting the iron isotopes analyses, contributing
482 significantly to the depth and scope of this research. We thank Dario Ferreira Sanchez for
483 technical support during beamline experiments at MicroXAS (SLS-PSI, #20161155)

484 **Open Research**

485 All data that support the findings of this study are available in Tables 1- 3 of this article, and in
486 the Supporting Information. In addition, the datasets for this research have been available in
487 Zenodo: DOI [will be included during revision round, and before publication, essentially all data
488 presented in Tables 1 to 3 and SI, contained in a single excel file].

489
490 ORCID Daniel Petrash: [0000-0001-5039-0543](https://orcid.org/0000-0001-5039-0543)

491 **References**

- 493 Archer C, Vance D (2006) Coupled Fe and S isotope evidence for Archean microbial Fe(III) and
494 sulfate reduction. *Geology* 34, 153–156.
- 495 Balci N, Shanks WC, Mayer B, Mandernack KW (2007) Oxygen and sulfur isotope systematics
496 of sulfate produced by bacterial and abiotic oxidation of pyrite, *Geochimica et*
497 *Cosmochimica Acta*, 71, 3796–3811.
- 498 Bayon, G., Bindeman, I. N., Trinquier, A., Retallack, G. J., & Bekker, A. (2022). Long-term
499 evolution of terrestrial weathering and its link to Earth’s oxygenation. *Earth and Planetary*
500 *Science Letters*, 584, 117490. doi: 10.1016/J.EPSL.2022.117490
- 501 Bouška, V., & Pešek, J. (1999). Quality parameters of lignite of the North Bohemian Basin in the
502 Czech Republic in comparison with the world average lignite. *International Journal of Coal*
503 *Geology*, 40(2–3), 211–235. doi: 10.1016/S0166-5162(98)00070-6
- 504 Brüchert, V. (2004). Physiological and ecological aspects of sulfur isotope fractionation during
505 bacterial sulfate reduction. *Special Paper of the Geological Society of America*, 379, 1–16.
506 doi: 10.1130/0-8137-2379-5.1
- 507 Busigny, V., Planavsky, N. J., Jézéquel, D., Crowe, S., Louvat, P., Moureau, J., Viollier, E., &
508 Lyons, T. W. (2014). Iron isotopes in an Archean ocean analogue. *Geochimica et*
509 *Cosmochimica Acta*, 133, 443–462. doi: 10.1016/j.gca.2014.03.004
- 510 Canfield, D. E. (2001). Biogeochemistry of Sulfur Isotopes. *Reviews in Mineralogy and*
511 *Geochemistry*, 43(1), 607–636. doi: 10.2138/GSRMG.43.1.607
- 512 Claff, S. R., Sullivan, L. A., Burton, E. D., & Bush, R. T. (2010). A sequential extraction
513 procedure for acid sulfate soils: Partitioning of iron. *Geoderma*, 155(3–4), 224–230. doi:
514 10.1016/J.GEODERMA.2009.12.002

- 515 Dreher, C. L., Schad, M., Robbins, L. J., Konhauser, K. O., Kappler, A., & Joshi, P. (2021).
 516 Microbial processes during deposition and diagenesis of Banded Iron Formations. *PalZ*
 517 *2021 95:4*, 95(4), 593–610. doi: 10.1007/S12542-021-00598-Z
- 518 Fakhraee, M., Hancisse, O., Canfield, D. E., Crowe, S. A., & Katsev, S. (2019). Proterozoic
 519 seawater sulfate scarcity and the evolution of ocean–atmosphere chemistry. *Nature*
 520 *Geoscience 2019 12:5*, 12(5), 375–380. doi: 10.1038/s41561-019-0351-5
- 521 Geissler, W. H. (2005). *Scientific Technical Report STR05/06: Seismic and Petrological*
 522 *Investigations of the Lithosphere in the Swarm-Earthquake and CO Degassing Region*
 523 *Vogtland/NW-Bohemia in der Helmholtz-Gemeinschaft*. Potsdam. doi: 10.2312/GFZ.b103-
 524 05063
- 525 Johnston, D. T., Gill, B. C., Masterson, A., Beirne, E., Casciotti, K. L., Knapp, A. N., &
 526 Berelson, W. (2014). Placing an upper limit on cryptic marine sulphur cycling. *Nature*,
 527 *513(7519)*, 530–533. doi: 10.1038/nature13698
- 528 Karimian, N., Johnston, S. G., & Burton, E. D. (2017). Antimony and Arsenic Behavior during
 529 Fe(II)-Induced Transformation of Jarosite. *Environmental Science and Technology*, *51(8)*,
 530 4259–4268. doi: 10.1021/ACS.EST.6B05335/SUPPL_FILE/ES6B05335_SI_001.PDF
- 531 Koeksoy, E., Halama, M., Konhauser, K. O., & Kappler, A. (2015). *Using modern ferruginous*
 532 *habitats to interpret Precambrian banded iron formation deposition*. doi:
 533 10.1017/S1473550415000373
- 534 Mach, K., Žák, K., Teodoridis, V., & Kvaček, Z. (2017). Consequences of Lower Miocene CO₂
 535 degassing on geological and paleoenvironmental settings of the Ahníkov/Merkur Mine
 536 paleontological locality (Most Basin, Czech Republic). *Neues Jahrbuch Für Geologie Und*
 537 *Paläontologie - Abhandlungen*, *285(3)*, 235–266. doi: 10.1127/NJGPA/2017/0680
- 538 Mills, J. V., Antler, G., & Turchyn, A. V. (2016). Geochemical evidence for cryptic sulfur
 539 cycling in salt marsh sediments. *Earth and Planetary Science Letters*, *453*, 23–32. doi:
 540 10.1016/J.EPSL.2016.08.001
- 541 Murad, E., & Rojík, P. (2005). Iron mineralogy of mine-drainage precipitates as environmental
 542 indicators: review of current concepts and a case study from the Sokolov Basin, Czech
 543 Republic. *Clay Minerals*, *40(4)*, 427–440. doi: 10.1180/0009855054040181
- 544 Murad, Enver, & Rojík, P. (2003). Iron-rich precipitates in a mine drainage environment:
 545 Influence of pH on mineralogy. *American Mineralogist*, *88(11-12 PART 2)*, 1915–1918.
 546 doi: 10.2138/am-2003-11-1234
- 547 Petrash, D. A., Jan, J., Sirová, D., Osafo, N. O.-A., & Borovec, J. (2018). Iron and nitrogen
 548 cycling, bacterioplankton community composition and mineral transformations involving
 549 phosphorus stabilisation in the ferruginous hypolimnion of a post-mining lake.
 550 *Environmental Science. Processes & Impacts*, *20(10)*, 1414–1426. doi:
 551 10.1039/c8em00328a
- 552 Petrash, D. A., Steenbergen, I. M., Valero, A., Meador, T. B., Paces, T., & Thomazo, C. (2022).
 553 Aqueous system-level processes and prokaryote assemblages in the ferruginous and sulfate-
 554 rich bottom waters of a post-mining lake. *Biogeosciences*, *19(6)*, 1723–1751. doi:
 555 10.5194/bg-19-1723-2022

- 556 Phillips, D. L. and Gregg, J. W. (2001). Uncertainty in source partitioning using stable isotopes.
557 *Oecologia*, 127, 171–179.
- 558 Posth, N. R., Canfield, D. E., & Kappler, A. (2014). Biogenic Fe(III) minerals: From formation
559 to diagenesis and preservation in the rock record. *Earth-Science Reviews*, 135, 103–121.
560 doi: 10.1016/j.earscirev.2014.03.012
- 561 Poulton, S. W., & Canfield, D. E. (2005). Development of a sequential extraction procedure for
562 iron: implications for iron partitioning in continentally derived particulates. *Chemical*
563 *Geology*, 214(3–4), 209–221. doi: 10.1016/J.CHEMGEO.2004.09.003
- 564 Raiswell, R., Hardisty, D. S., Lyons, T. W., Canfield, D. E., Owens, J. D., Planavsky, N. J.,
565 Poulton, S. W., & Reinhard, C. T. (2018). The iron paleoredox proxies: A guide to the
566 pitfalls, problems and proper practice. *American Journal of Science*, 318(5), 491–526. doi:
567 10.2475/05.2018.03
- 568 Rapprich, V., Čáp, P., Erban Kochergina, Y. V., Kadlecová, E., Benkó, Z., Sakala, J., Rodovská,
569 Z., Matějů, J., & Petrash, D. A. (2023). Interactions between distal epiclastic and bio-
570 chemogenic sedimentation at the foothills of a mafic alkaline volcano: The case of the
571 Oligocene Doupovské Hory Volcanic Complex (Czech Republic). *Depositional Record*,
572 9(4), 871–894. doi: 10.1002/dep2.240
- 573 Rojík, P. (2004). New stratigraphic subdivision of the Tertiary in the Sokolov Basin in
574 Northwestern Bohemia. *Journal of the Czech Geological Society*, 49(3–4), 173–185.
- 575 Saunders, J. K., Fuchsman, C. A., McKay, C., & Rocoap, G. (2019). Complete arsenic-based
576 respiratory cycle in the marine microbial communities of pelagic oxygen-deficient zones.
577 *Proceedings of the National Academy of Sciences of the United States of America*, 116(20),
578 9925–9930. doi: 10.1073/PNAS.1818349116/SUPPL_FILE/PNAS.1818349116.SAPP.PDF
- 579 Scholz, F. (2018). Identifying oxygen minimum zone-type biogeochemical cycling in Earth
580 history using inorganic geochemical proxies. *Earth-Science Reviews*, 184(August), 29–45.
581 doi: 10.1016/j.earscirev.2018.08.002
- 582 Swanner, E. D., Lambrecht, N., Wittkop, C., Harding, C., Katsev, S., Torgeson, J., & Poulton, S.
583 W. (2020). The biogeochemistry of ferruginous lakes and past ferruginous oceans. *Earth-*
584 *Science Reviews*, 103430. doi: 10.1016/j.earscirev.2020.103430
- 585 Umbría-Salinas, K., Valero, A., Jan, J., Borovec, J., Chrastný, V., & Petrash, D. A. (2021).
586 Redox-driven geochemical partitioning of metal(loid)s in the iron-rich anoxic sediments of
587 a recently flooded lignite mine pit: Lake Medard, NW Czechia. *Journal of Hazardous*
588 *Materials Advances*, 3, 100009. doi: 10.1016/j.hazadv.2021.100009
- 589 Valero, A., Jan, J., & Petrash, D. (2023). Anaerobic dissolved As(III) removal from metal-
590 polluted waters by cathode-stabilized Fe(III)-oxyhydroxides. *Environmental Science: Water*
591 *Research & Technology*. doi: 10.1039/D2EW00844K
- 592 van de Velde, S. J., Reinhard, C. T., Ridgwell, A., & Meysman, F. J. R. (2021). Bistability in the
593 redox chemistry of sediments and oceans. *Proceedings of the National Academy of Sciences*
594 *of the United States of America*, 117(52), 33043–33050. doi: 10.1073/PNAS.2008235117
- 595 Weinlich, F. H., Bräuer, K., Kämpf, H., Strauch, G., Tesar, J., & Weise, S. M. (1999). An active
596 subcontinental mantle volatile system in the western Eger rift, Central Europe: Gas flux,

597 isotopic (He, C, and N) and compositional fingerprints. *Geochimica et Cosmochimica Acta*,
598 63(21), 3653–3671. doi: 10.1016/S0016-7037(99)00187-8

599 Zerkle, A. L., Jones, D. S., Farquhar, J., & Macalady, J. L. (2016). Sulfur isotope values in the
600 sulfidic Frasassi cave system, central Italy: A case study of a chemolithotrophic S-based
601 ecosystem. *Geochimica et Cosmochimica Acta*, 173, 373–386. doi:
602 10.1016/J.GCA.2015.10.028

603

604 **Figure 1.** Redox-driven solubility and mobility patterns in LM's bottom water column: (a).
605 Redox potential, pH and conductivity variations with increasing water column depths. (b).
606 Profiles of dissolved Fe and Mn concentrations. (c-d). Increasing trends in dissolved, As, V, and
607 REE concentrations are likely regulated by the reductive dissolution of Fe(III) and Mn(IV,III)
608 oxyhydroxides sinks, occurring diffusively from sedimentary sources (and water column sinks).
609 (d). The reductive dissolution of phases with a high affinity for light REEs (LREEs) in
610 sediments, and their subsequent re-complexation with Fe(III)-bearing colloids in solution allow
611 for the persistence of heavy REEs (HREEs) until their precipitative removal in the dysoxic
612 hypolimnion (at above 49 m depth).

613 **Figure 2.** Geochemical gradients in LM's stratified water column: (a). Fe concentration profiles
614 and $\delta^{56}\text{Fe}$ isotopic values. (b). Dissolved inorganic carbon (DIC) concentrations alongside $\delta^{13}\text{C}$
615 values. (c). Sulfate concentrations with $\delta^{34}\text{S}$ values of dSO_4^{2-} .

616 **Figure 3.** Mineralogical Analyses Part 1: (a-b). Microscopic features of S-bearing mineral in LM
617 sediments, captured using scanning electron microscopy (SEM). Panel (a) showcases equant
618 gypsum microcrystals and panel (b) exhibits an accessory pyrite microcrystal. (c). Semi-
619 quantitative results derived from X-ray diffraction (XRD). The Rietveld refinement method was
620 employed to enhance the precision of phase identification and quantification, providing insights
621 into the mineralogical composition of the analyzed samples (d). X-ray Absorption Near-Edge
622 Structure (XANES) of bulk sediments: The inset highlights the spectral characteristics at the pre-
623 edge region. The spectrum is predominantly characterized ($90 \pm 4\%$ fit) by two components in an
624 octahedral coordination environment: goethite > lepidocrocite, which together account for 74–
625 79% of the total variance in the Fe-bearing phases. An additional 26–21% is attributable to
626 Fe(II)-bearing, mixed-valence hercynite ($\text{Fe}^{2+,3+}\text{Al}_2\text{O}_4$) clay as a third significant component.

627 **Figure 4.** Eh-pH (Pourbaix) diagram depicting the behavior of Fe (a) and sulfate (b) species
628 below the redoxcline in LM. This diagram goes beyond Eh and pH, incorporating temperature
629 and major element concentrations as influencing factors (for details, see Table 1). With
630 increasing Eh at greater depths, the arrangement of points reflects a depth-dependent perspective,
631 elucidating potential shifts in equilibrium phases within the dynamic hydrochemistry of LM.
632 Crosses on the diagram indicate samples taken at maximal Eh ranges, while dots represent water
633 column measurements when the monimolimnion Eh was at more prevalent -210 mV.

634 **Figure 5.** Mineralogical analyses. Part 2: (a). Concentrations of Fe (wt%), and Mn, V, As, and
635 the sum of lanthanides (mg kg^{-1}) in sediment samples, determined post sequential extraction and
636 spectroscopic analysis of extracts. (b). Proportional distribution of metal(loid) fractions in the
637 reactive Fe phases considered, determined as a fraction of total Fe. (c). Application of REE

638 systematics to cerium-lanthanum anomalies, highlighting the pronounced variation in anomalies
639 within reactive Fe(III)-oxyhydroxide phases compared to more consistent trends in carbonates
640 influenced by the same redox buffering effect of the overlying ferruginous and sulfatic water
641 column. (d). Scanning electron microscopy (SEM) images illustrating FeOOH aggregate
642 abundance and texture in the upper anoxic LM's sediments. Other phases often observed are
643 kaolinite, K-feldspar, muscovite and detrital siderite (arrow) (e): backscattered SEM detail of the
644 analytical area shown in “(d)” showing an organo-mineral FeOOH aggregate.

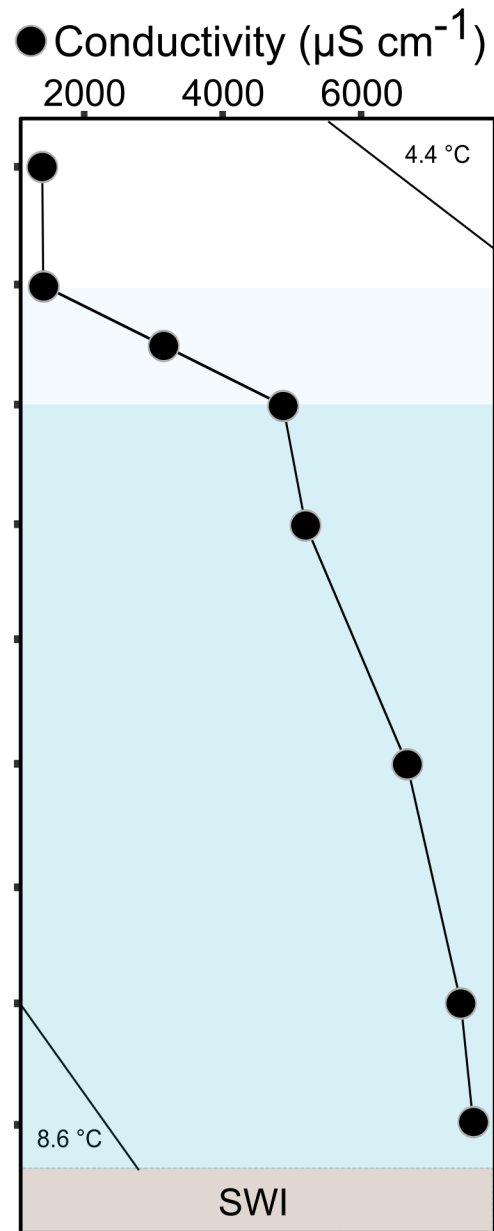
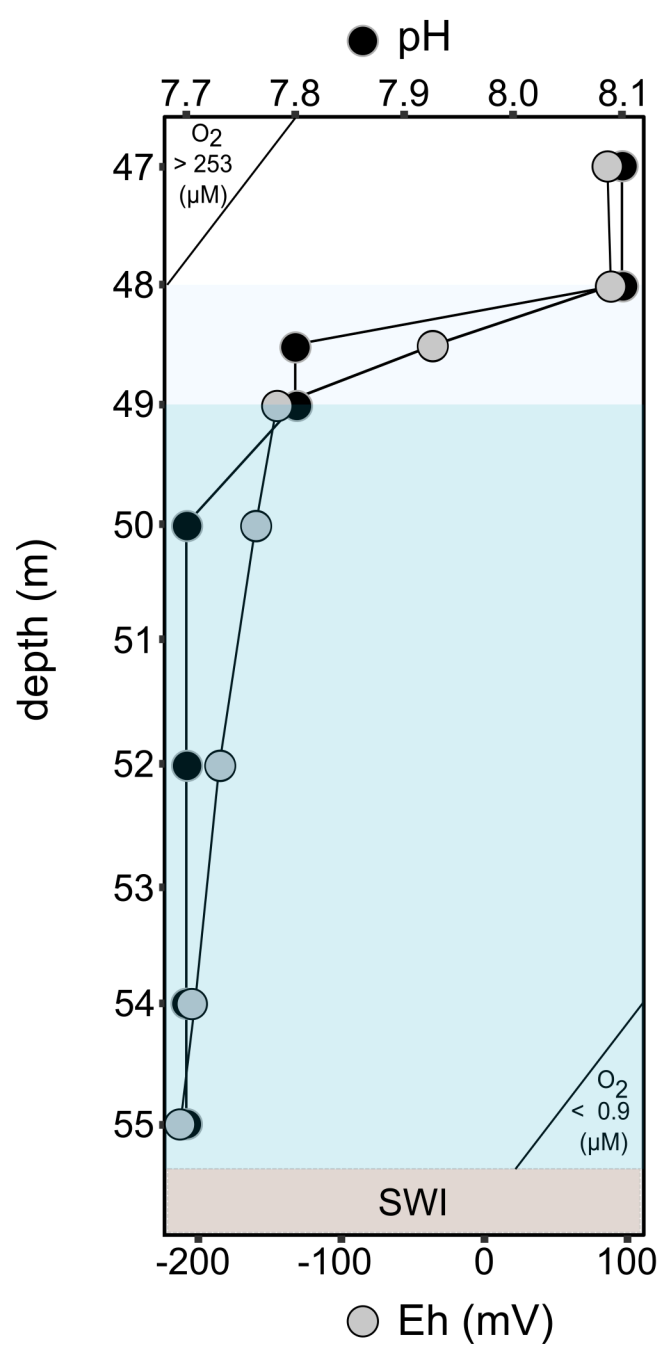
645 **Table 1.** Dissolved concentrations of manganese (Mn^{2+}) and dissolved concentrations and stable
646 isotope ratios of iron (Fe^{2+}), inorganic carbon (i.e., $\Sigma\text{CO}_2 = \text{H}_2\text{CO}_3 + \text{HCO}_3^- + \text{CO}_3^{2-}$) and sulfate
647 (SO_4^{2-}) at the central deepest part of LM (47 to 55 m depth below the surface). The
648 corresponding physicochemical parameters and dissolved trace metal contents pertaining the
649 sampled bottom water column are shown in the Supporting Information, Table S1

650 **Table 2.** Concentrations of Al, Fe (wt%), and Mn, V, As, the sum of lanthanides, and redox
651 sensitive Ce (mg kg^{-1}), along with Ce anomalies (Ce^*) in LM's anoxic sediment cores from 0 to
652 8 cm depth. These concentrations were determined after sequential extraction and spectroscopic
653 analysis of the extracts. Sediment samples were collected under varying Eh conditions in the
654 overlying bottom water column, specifically from monimolimnion layers at -180 and -90 mV.
655 TOC values, exhibiting minor variability, are further detailed in the footnote of this table.

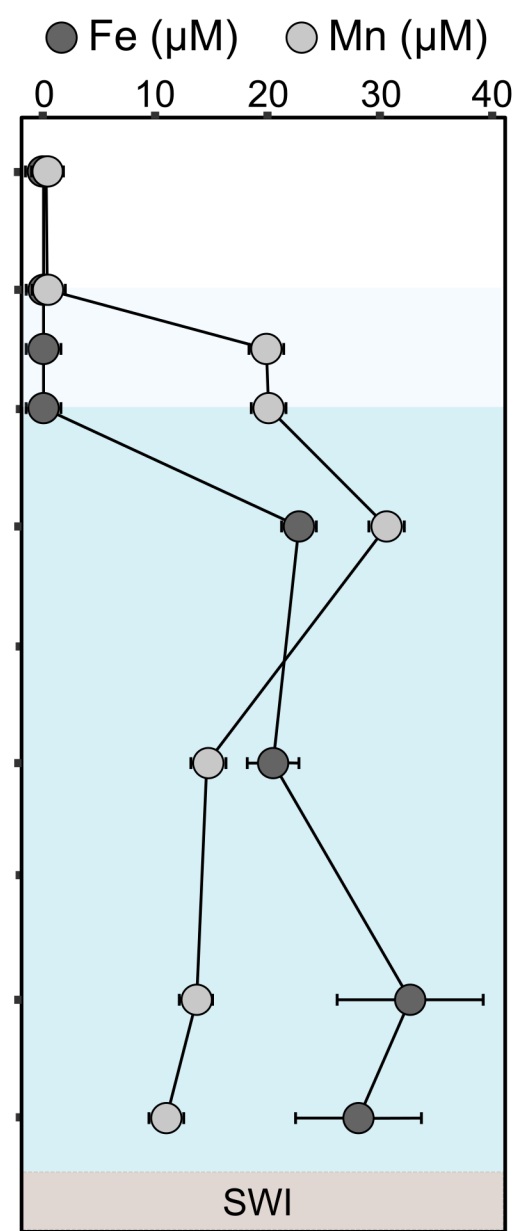
656 **Table 3.** Saturation indices ($\log(\text{IAP}/\text{K}_{\text{sp}})$) estimated for various minerals in theoretical
657 equilibrium with LM's bottom water column at two distinct peak mean monimolimnial's redox
658 potentials (i.e., -210 and -80 mV).

Figure 1.

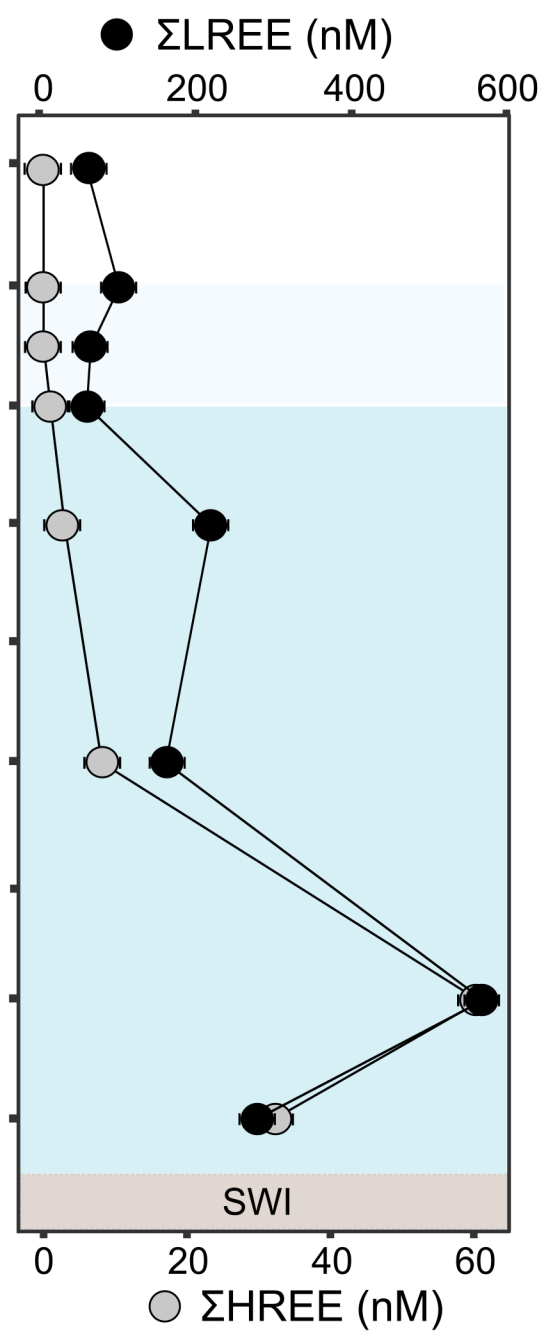
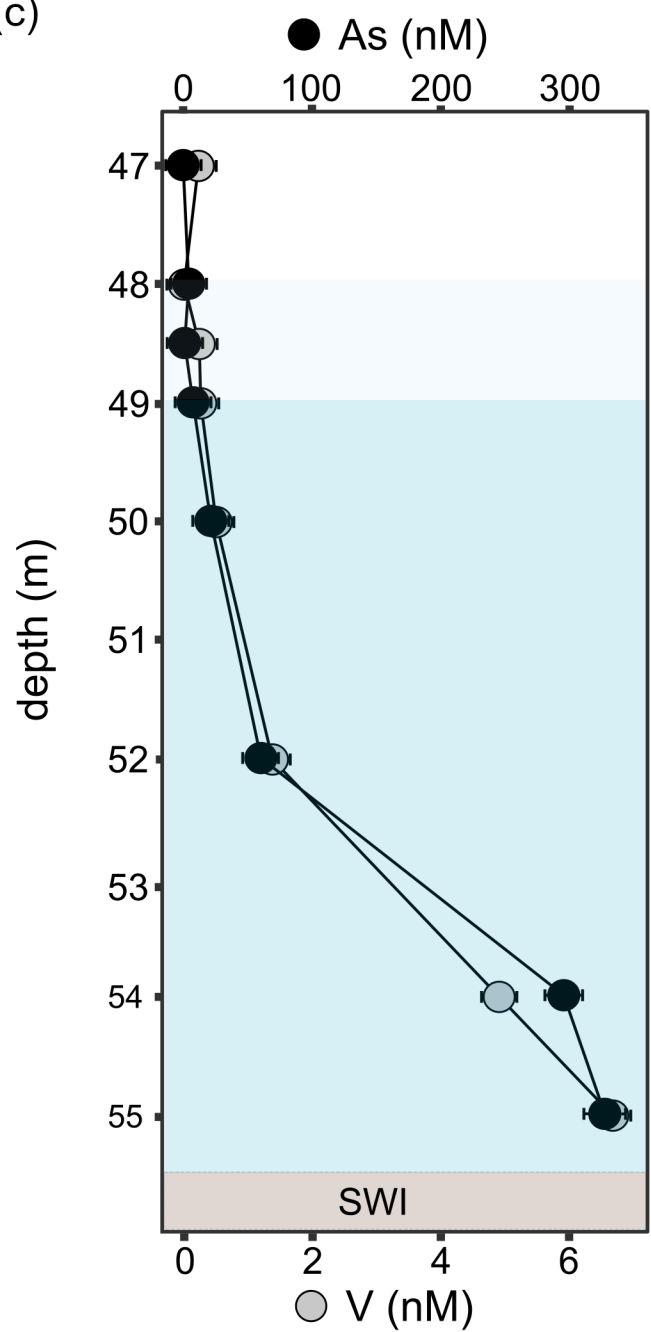
(a)



(b)



(c)



(d)

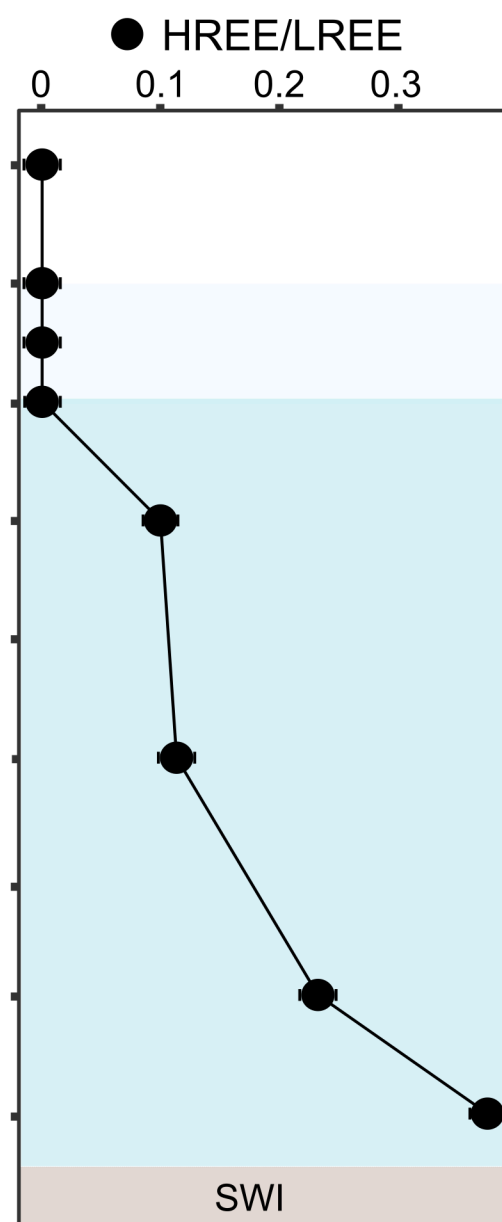


Figure 2.

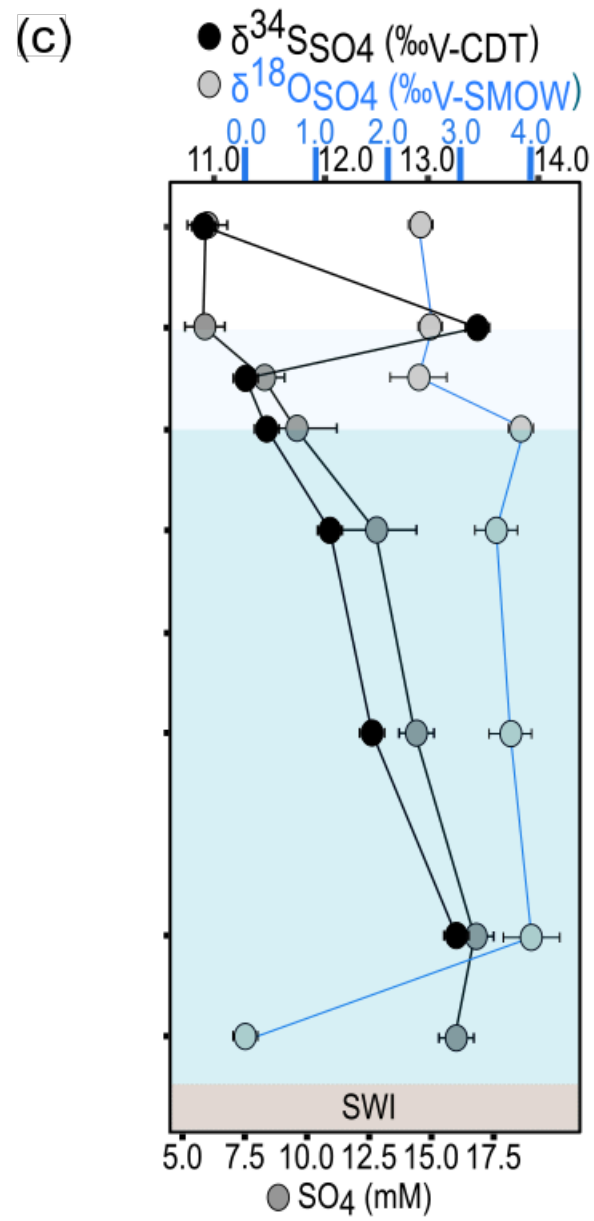
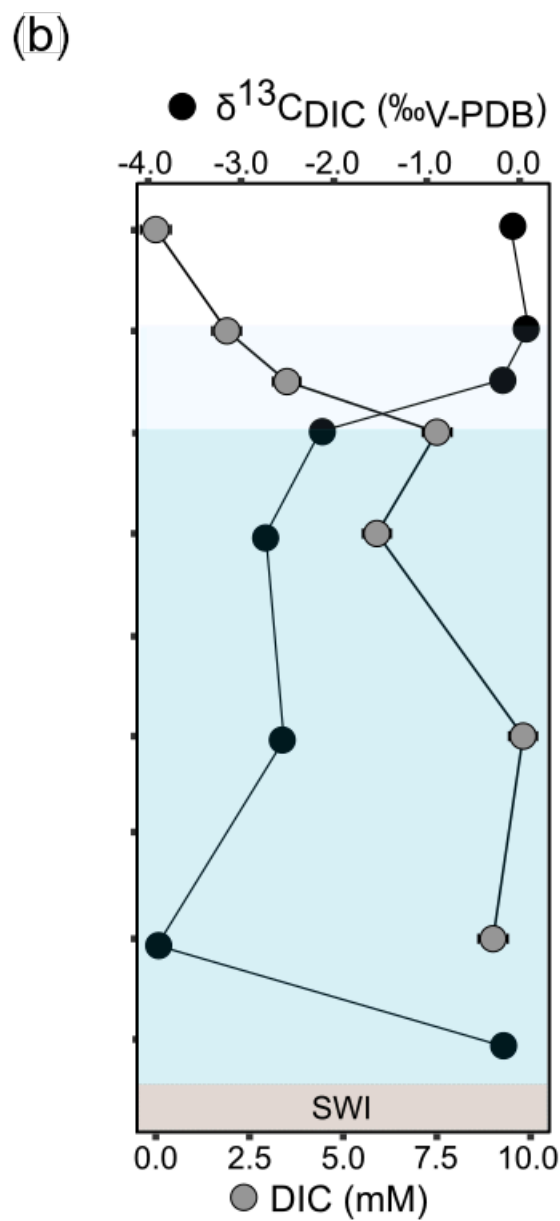
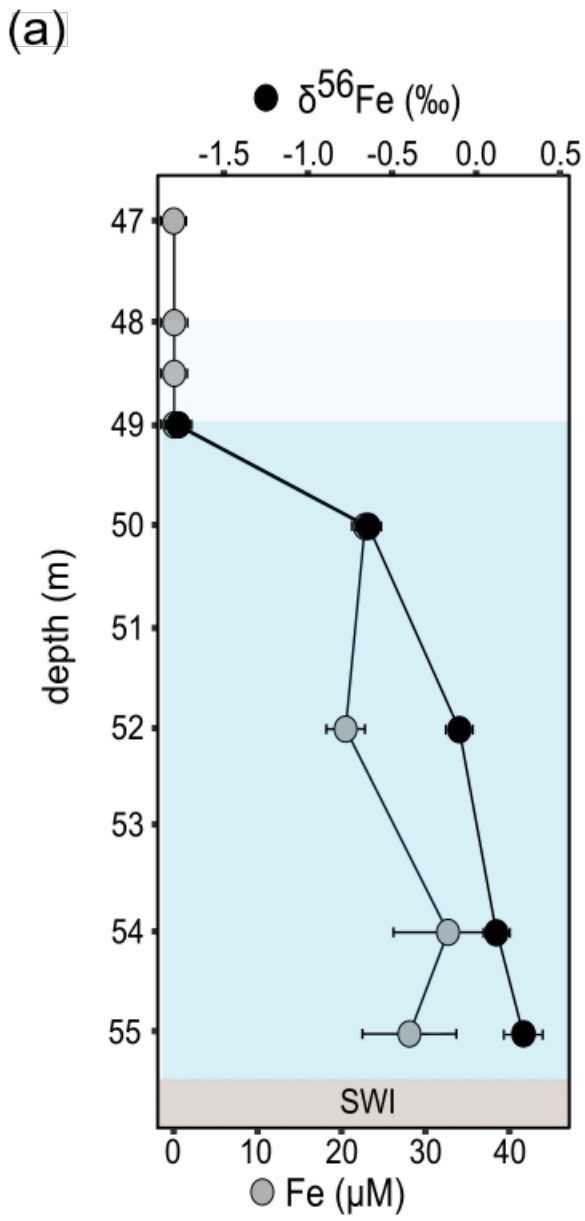


Figure 3.

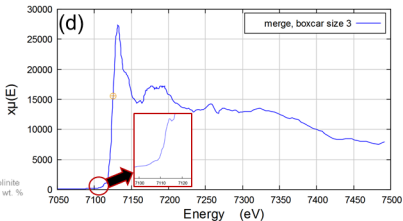
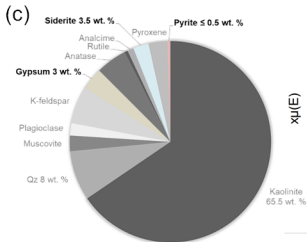
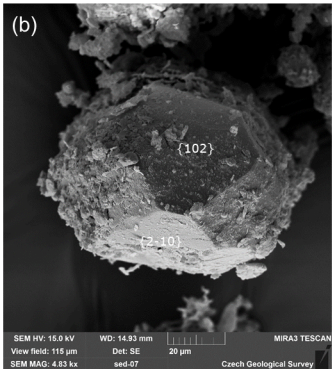
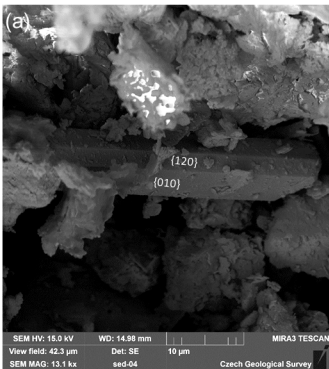


Figure 4.

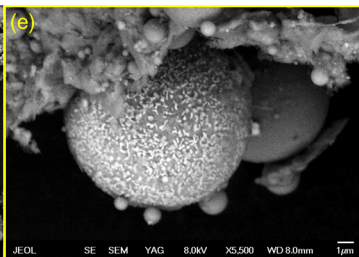
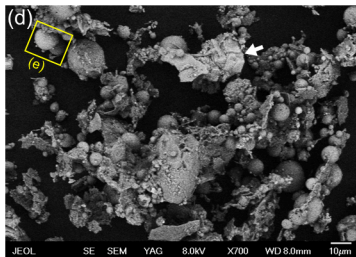
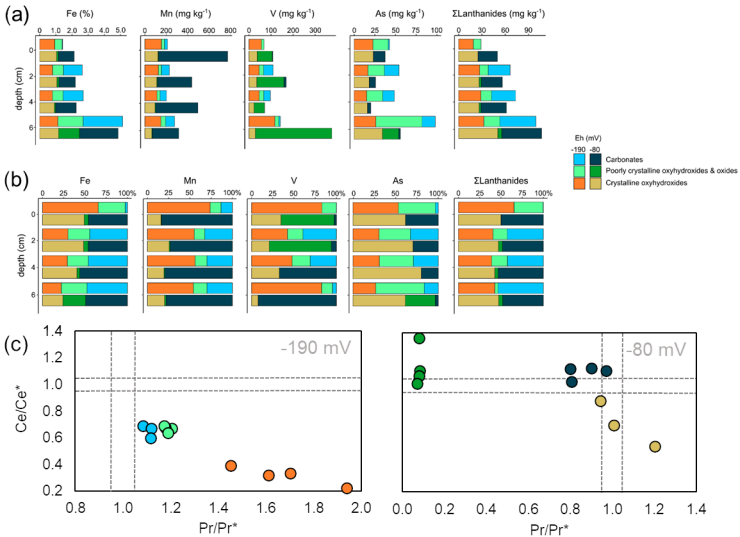
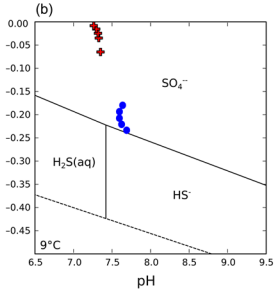
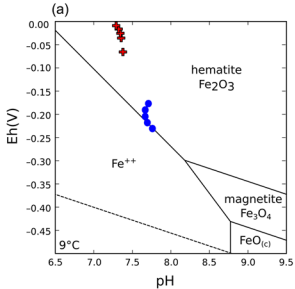


Figure 5.



1 **Table 1.** Dissolved concentrations of manganese (Mn^{2+}) and dissolved concentrations and stable isotope ratios of iron (Fe^{2+}), inorganic carbon
2 (i.e., $\Sigma\text{CO}_2 = \text{H}_2\text{CO}_3 + \text{HCO}_3^- + \text{CO}_3^{2-}$) and sulfate (SO_4^{2-}) at the central deepest part of LM (47 to 55 m depth below the surface). The
3 corresponding physicochemical parameters and dissolved trace metal contents pertaining the sampled bottom water column are shown in the
4 Supplementary Material 1, Table SM1

Depth (m)	Mn^{2+} (μM)	Fe^{2+} (μM)	$\delta^{56}\text{Fe}$ (‰)	DIC (mM)	$\delta^{13}\text{C}$ (‰) _{VPDB}	SO_4^{2-} (mM)	$\delta^{34}\text{S}-\text{SO}_4^{2-}$ (‰) _{VCDT}	$\delta^{18}\text{O}-\text{SO}_4^{2-}$ (‰) _{VSMOW}
47	0.33 ± 0.01	0.07 ± 0.01	nd.	nd.	nd.	6.00 ± 0.80	$+10.90 \pm 0.10$	nd.
48	0.42 ± 0.01	0.07 ± 0.01	nd.	1.90 ± 0.10	$+0.20 \pm 0.05$	5.90 ± 0.80	$+13.50 \pm 0.07$	$+13.20 \pm 0.20$
48.5	19.92 ± 0.36	0.07 ± 0.01	nd.	3.50 ± 0.20	-0.10 ± 0.05	8.30 ± 0.80	$+11.30 \pm 0.03$	$+13.10 \pm 0.05$
49	20.11 ± 0.36	0.07 ± 0.01	-01.77 ± 0.03	7.50 ± 0.10	-2.10 ± 0.03	9.60 ± 1.60	$+11.50 \pm 0.10$	$+14.20 \pm 0.10$
50	30.57 ± 0.55	22.80 ± 0.40	-0.64 ± 0.08	5.90 ± 0.10	-2.70 ± 0.10	12.80 ± 1.60	$+12.10 \pm 0.10$	$+12.70 \pm 0.40$
52	14.62 ± 0.26	20.50 ± 2.30	-0.10 ± 0.05	9.80 ± 0.20	-2.50 ± 0.10	14.40 ± 0.70	$+12.50 \pm 0.10$	$+13.80 \pm 0.20$
54	13.72 ± 0.25	32.70 ± 6.50	$+0.12 \pm 0.05$	9.00 ± 0.20	-3.90 ± 0.40	16.80 ± 0.70	$+13.30 \pm 0.10$	$+13.20 \pm 1.10$
55	11.08 ± 0.20	28.10 ± 5.60	$+0.27 \pm 0.10$	nd.	nd.	16.00 ± 0.70	nd.	nd.

5 nd.: Not determined

6 **Table 2.** Concentrations of Al, Fe (wt%), and Mn, V, As, the sum of lanthanides, and redox sensitive Ce (mg kg⁻¹), along with Ce anomalies (Ce*) in LM's
7 anoxic sediment cores from 0 to 8 cm depth. These concentrations were determined after sequential extraction and spectroscopic analysis of the extracts.
8 Sediment samples were collected under varying Eh conditions in the overlying bottom water column, specifically from monimolimnion layers at -180 and -90
9 mV. TOC values, exhibiting minor variability, are further detailed in the footnote of this table.

Depth range (cm)	Fraction	Fe (wt. %)		Mn (mg kg ⁻¹)		V (mg kg ⁻¹)		As (mg kg ⁻¹)		ΣREE (mg kg ⁻¹)		Ce (mg kg ⁻¹)		Ce*	
		-190 mV	-80 mV	-190 mV	-80 mV	-190 mV	-80 mV	-190 mV	-80 mV	-190 mV	-80 mV	-190 mV	-80 mV	-190 mV	-80 mV
0-2	Carbonates	0.04	0.98	28.18	646.01	<L.Q	2.88	1.42	14.45	0.10	25.01	0.10	10.99	nd.	1.32
	Poorly crystalline oxyhydroxides	0.93	1.05	156.38	123.68	56.61	37.59	22.72	23.10	18.92	24.91	6.04	11.44	0.79	1.30
	Crystalline oxyhydroxides	0.45	0.10	26.95	4.63	11.70	67.84	18.50	<L.Q	9.87	<L.Q	1.15	<L.Q	0.45	nd.
2-4	Carbonates	1.17	1.02	74.46	321.63	43.14	10.10	17.64	7.71	28.26	27.14	9.01	11.81	0.79	1.29
	Poorly crystalline oxyhydroxides	0.79	1.07	126.43	112.12	46.36	35.26	16.58	18.17	27.00	26.51	8.81	12.92	0.77	1.92
	Crystalline oxyhydroxides	0.67	0.12	28.55	5.36	19.98	123.29	19.98	<L.Q	11.20	2.56	2.07	1.03	0.41	0.90
6-8	Carbonates	1.24	1.27	60.61	394.91	30.02	<L.Q	14.19	4.05	31.01	32.89	9.52	14.72	0.80	1.30
	Poorly crystalline oxyhydroxides	0.79	0.91	113.46	96.13	46.44	23.12	15.09	16.09	28.66	26.44	9.57	12.04	0.79	1.24
	Crystalline oxyhydroxides	0.67	0.07	28.18	4.48	20.69	47.48	19.34	<L.Q.	13.75	2.33	2.53	0.79	0.49	0.71

10 TOC values decrease with increasing depth, remaining within the analytical error for both sediment sampling campaigns. They range from 5.1 ± 0.2
11 (at the SWI) to 3.7 ± 0.4 (at a sediment pile depth of 6-8 cm). The TOC predominantly consists of refractory lignitic particles. The repeatability of the
12 core analyses, expressed as the relative standard deviation, varies for different elements. For V, Mn, and Fe, the repeatability ranges from 4.4% to
13 9.0%; for As, it ranges from 8.3% to 10.6%; and for REE, it ranges from 1.5% to 10.8%; all percentages being relative to the reported values. <L.Q.:
14 less than the quantification limit

15 **Table 3.** Saturation indices (log (IAP/K_{sp})) estimated for various minerals in theoretical equilibrium with LM's bottom water column at two distinct
 16 monimolimnial's redox potentials (i.e., -190 and -80 mV)

Mineral	Sat. Index*		Mineral	Sat. Index *	
	-190 mV	-80 mV		-190 mV	-80 mV
Al(OH) ₃ (am)	0.786	0.328	Huntite	-0.205	0.597
Al ₂ O ₃ (s)	3.165	2.141	Hydroxyapatite	4.066	2.49
Anhydrite	-1.814	-1.823	Lepidocrocite	8.586	9.271
Aragonite	-0.564	-0.329	Mackinawite	-1.163	-0.363
Brucite	-3.561	-2.42	Magnesite	0.889	1.232
Ca ₃ (PO ₄) ₂ (beta)	-1.598	-2.972	Magnetite	24.919	27.777
CaCO ₃ xH ₂ O(s)	-1.747	-1.498	MnCO ₃ (am)	-0.882	-0.041
Calcite	-0.408	-0.17	MnHPO ₄ (s)	1.006	0.113
Chalcedony	0.21	0.201	Na-Jarosite	2.433	1.814
Cristobalite	0.013	0.005	Pyrite	6.746	12.621
Diaspore	4.792	4.356	Quartz	0.686	0.685
Dolomite (disordered)	0.503	0.908	Rhodochrosite	-0.4	0.435
Fe(OH) ₂ (c)	-2.44	-0.354	Sepiolite (A)	-0.069	2.672
Fe ₃ (OH) ₈ (s)	10.14	13.596	Siderite	-0.455	0.428
Ferrihydrite	5.772	6.169	SiO ₂ (am)	-0.645	-0.667
FeS (ppt)	-1.921	-1.152	Spinel	-0.642	-0.568
Gibbsite (C)	3.905	3.464	Strengite	1.828	-0.429
Goethite	8.873	9.383	Struvite	-2.818	-3.508
Gypsum	-1.486	-1.471	Variscite	0.216	-2.867
Hematite	20.069	21.068	Vaterite	-1.019	-0.793
H-Jarosite	-4.352	-5.783	Vivianite	0.282	0.727

17 *Calculated by using the Visual Minteq 3.1 code with the following input values: temperature = 9.2/4.8 °C, pH = 7.7/8.2, ionic strength = 0.06/0.04 M, O₂ = 0.002/0.06 mM,
 18 Alkalinity (as HCO₃⁻) = 177/147 mg L⁻¹, DOC = 12 mg L⁻¹, DIC = 9.0 mM, Na⁺ = 24.0/17.0 mM, K⁺ = 0.31/0.27 mM, Ca²⁺ = 4.0/3.7 mM, Mg²⁺ = 445.0 mM, Si = 0.29/0.25
 19 mM, Al³⁺ = 0.05 mM, Fe²⁺ = 0.028/0.117 mM, Fe³⁺ = 0.172/0.131 mM, Mn²⁺ = 0.011/0.040 mM, PO₄³⁻ = 0.02/0.001 mM, SO₄²⁻ = 16.0/20.0 mM, HS⁻ = 0.00025 mM, NO₃⁻ =
 20 0.017/0.040 mM, and NH₄⁺ = 0.127/0.142 mM for -190 mV and -80 mV, respectively.